frontiers | Frontiers in Earth Science

TYPE Original Research
PUBLISHED 10 September 2025
DOI 10.3389/feart.2025.1573046

OPEN ACCESS

EDITED BY
Derek Keir,
University of Southampton, United Kingdom

REVIEWED BY
Pura Alfonso,
Universitat Politecnica de Catalunya, Spain
Yinhang Cheng,
Tianjin Center of Geological Survey, China Geological Survey, China
Alexander U. Falster,
Maine Mineral & Gem Museum, United States

*CORRESPONDENCE
Yong Tang,
tangyong@yip.gyig.ac.cn

†These authors share first authorship

RECEIVED 08 February 2025
ACCEPTED 11 August 2025
PUBLISHED 10 September 2025

CITATION
Wang H, Ren G, Tang Y, Zhang H, Lv Z and Huang Z (2025) Exhumation of the Koktokay rare-metal pegmatite group in the China Altai: insights from low-temperature thermochronology of the No. 3 pegmatite and Aler S-type granitic batholith. *Front. Earth Sci.* 13:1573046. doi: 10.3389/feart.2025.1573046

Exhumation of the Koktokay rare-metal pegmatite group in the China Altai: insights from low-temperature thermochronology of the No. 3 pegmatite and Aler S-type granitic batholith

Haoyu Wang[1,2†], Guangming Ren[1†], Yong Tang[2]*, Hui Zhang[2], Zhenghang Lv[2] and Zhilong Huang[2]

[1]Chengdu Center of China Geological Survey (Geoscience Innovation Center of Southwest China), Chengdu, Sichuan, China, [2]State Key Laboratory for Critical Mineral Research and Exploration, Institute of Geochemistry, Chinese Academy of Sciences, Guiyang, China

The China Koktokay Pegmatite Group is an important metallogenic region where major rare-metal ores are mined. Here, we present new low-temperature thermochronological data to contribute to the understanding of the Koktokay Pegmatite Group's exhumation and preservation history. Apatite U–Pb ages of ~176 Ma, zircon fission-track ages of ~150 Ma, zircon (U–Th)/He ages of ~82–52 Ma, apatite fission-track ages of ~69–49 Ma, and apatite (U–Th)/He ages of ~90–52 Ma were obtained from three samples of the No. 3 pegmatite and the contemporaneous Aler granitic batholith in the Koktokay area. Our thermochronological data and inverse thermal history modeling reveal a moderate-to-rapid basement cooling phase during the Cretaceous (~150–65 Ma), with an average cooling rate of ~1.53 °C–1.06 °C/Ma. It is envisaged that this phase eventually uplifted and exhumed the pegmatite group, with erosion in the Cenozoic era being limited. Combined with previously published geochronological and thermochronological data, a multi-stage cooling history for the pegmatite group can be established. Following its magmatic–hydrothermal formation in the Late-Triassic (~220–200 Ma), two phases of accelerated regional cooling (i.e., in the late Triassic to Early Jurassic, ~200–180 Ma; and the mid-Jurassic to Late Jurassic, ~176–150 Ma) can be recognized. The intense cooling in the Cretaceous is associated with the final exhumation of the pegmatite group to the surface, and some Li–Ru–Cs-mineralized pegmatites formed at the distal end of the Koktokay Pegmatite Group may have been exhumed and denuded. Furthermore, we propose a relatively intense denudation of the Koktokay Pegmatite Group, which is unfavorable for the preservation of rare-metal pegmatite bodies.

KEYWORDS

China Altay, low-temperature thermochronology, pegmatite, (U–Th)/He age dating, fission track of apatite and zircon

1 Introduction

The preservation of ore deposits is an essential component of the mineralization system. The formation of an economic mineral deposit requires both a genetic process and subsequent exhumation events that enable commercial mining (Zhai et al., 2000; Kesler and Wilkinson, 2006). Therefore, understanding the erosion and uplift of deposits, mining areas, and larger regions not only contributes to the understanding of deposit preservation but also provides valuable information for regional deposit prospecting. Low-temperature thermochronological tools can determine the timing and rates at which a geo-body approaches the upper crust and surface and subsequently cools as a result of exhumation. Hence, these tools place constraints on the thermal history of a geo-body as it passes through a shallow crustal isothermal structure, undergoing cooling from ~450 to ~45 °C, and are used to reveal the complex dynamic mechanisms involved in the preservation of the geo-body (Reiners and Brandon, 2006; Enkelmann and Garver, 2016). Low-temperature thermochronology is majorly used to reconstruct the post-mineralization thermal history of deposits (Marton et al., 2010). It is useful for evaluating the preservation potential of deposits. Furthermore, when combined with medium- to high-temperature geo-/thermochronometry tools, such as apatite U–Pb, muscovite ^{40}Ar–^{39}Ar, and zircon U–Pb, a comprehensive history of cooling/preservation since the formation of the ores can be reconstructed (Evans et al., 2013; Zhang L. et al., 2017; Zhang J. et al., 2017).

Pegmatites have long received considerable attention due to their colorful gemstones, fine mineral specimens, and industrial minerals, such as feldspar and quartz. Additionally, pegmatites are significant reservoirs of rare metal elements (Linnen et al., 2014; Glover et al., 2012; Linnen et al., 2012; Simmons et al., 2012; London, 2008). London (2008) proposed a definition for pegmatite that provides a comprehensive overview of its characteristics. According to the definition, granitic pegmatite is an essentially igneous rock commonly granitic in composition. Fundamentally, pegmatite is distinguished from other igneous rocks by its extremely coarse, variable grain size or by the abundance of crystals with skeletal, graphic, or other strongly directional growth habits. Furthermore, pegmatites typically occur as a cluster, and within a pegmatite field, the distribution of rare-metal-mineralized pegmatites follows a systematic pattern reflecting their geochemical and textural evolution: microcline-rich pegmatites are found abundantly in the center, while Ta-, Li-, Rb-, and Cs-bearing minerals increase in abundance toward the outermost parts (Jahns and Burnham, 1969; Černý, 1991; Dill et al., 2012; London, 2018; Zhang and Li, 2024). For instance, within a pegmatite group, Be-mineralized pegmatites typically form near the center, while Li–Rb–Cs-mineralized pegmatites are found at the periphery (London, 2018), such as the Oxford pegmatite Field in Maine (Webber et al., 2019; Simmons et al., 2020). Therefore, determining the preservation status and erosion thickness is crucial for evaluating the potential for exploration of hidden ore bodies in pegmatite groups. However, there are only a few case studies on the preservation history of pegmatites, such as the Jiajika pegmatite in China (Liu et al., 2023).

The Altai Orogen, located in the western part of the Central Asian Orogenic Belt (CAOB) (Figure 1a), stretches approximately 2,500 km from Russia and Kazakhstan through China to Mongolia. The Altai Orogen is a significant producer of rare metals globally, with abundant rare-metal-mineralized pegmatites. It is referred to as the Kalba–Narym–Koktokay rare-metal (Li–Be–Nb–Ta–Cs) pegmatite belt (Annikova et al., 2016a; Annikova et al., 2016b; Murzintsev et al., 2019; Khromykh et al., 2020). The Koktokay Pegmatite Group, located in the central part of the Chinese Altai, is the characteristic rare-metal-producing area with massive contents of mineralized pegmatites. In the Koktokay Pegmatite Group, the dominant mineral is beryllium (Be). The most famous, No. 3 pegmatite, which contains 10 internal zones and vast resources of Be–Nb–Ta–Li, consists of large amounts of beryllium but moderate amounts of lithium (Zou and Li, 2006). Previous studies have primarily focused on the chronology, geodynamic processes, internal evolution, and mineralization of the Koktokay Pegmatite Group (Wang et al., 2007; Tang et al., 2018; Zhao and Yan, 2023; Shen et al., 2022; Zhang and Li, 2024). However, little attention has been paid to their long-term post-mineralization evolution (i.e., their exhumation and preservation). Exhumation and preservation of the ore-bearing bodies in the area remain poorly understood, which is important for mineral exploration.

It is clear that understanding the exhumation history of the Koktokay Pegmatite Group has valuable implications for gaining deeper insights into the preservation and exposure of the pegmatite group. We focus on the thermal history of the Koktokay Pegmatite Group. Moreover, the contemporaneous Aler granitic batholith in the Koktokay area is used as a reference for evaluating the preservation history. Pegmatite and granite samples are analyzed using medium- and low-temperature thermochronological techniques, including apatite U–Pb, zircon fission track (ZFT), zircon (U–Th)/He (ZHe), apatite fission track (AFT), and apatite (U–Th)/He (AHe). Their integrated thermal history is then derived through inverse modeling. In addition, based on compiled thermochronological data of this area, we further discuss the preservation history of the Koktokay pegmatite to shed more light on mineral exploration and provide a case study on pegmatite preservation research.

1.1 Geological setting

The Altai region occupies a key position within the CAOB (Figure 1a). It originated in the Late Paleozoic and is the result of the conglomeration of various geological entities, such as island arcs, accretionary wedges, seamounts, and microcontinents, during the Cambrian–Carboniferous period of the ancient Asian oceanic system (Buslov et al., 2001; Buslov et al., 2004; Windley et al., 2007; Glorie et al., 2011). Based on isotopic studies and the formation of a series of rift basins such as Ashele, Chongkuer, Kelan, and Maizi basins, a foreland basin developed in the southern part of the China Altai, characterized by extensional tectonic settings that persisted at least until the Late Carboniferous (Yuan et al., 2007). During this period, a limited amount of syn-orogenic pegmatite was formed, predominantly exposed in the Qiongkuer domain of the Altai, with small quantities and scale of rare-metal mineralization (Lv et al., 2018). The Carboniferous suturing between the Altai and the Junggar terranes is represented by the Irtysh Shear Zone (Figure 1b; Laurent-Charvet et al., 2002; Briggs et al., 2007). Despite the prolonged tectonic activity during the Mesozoic–Cenozoic, the

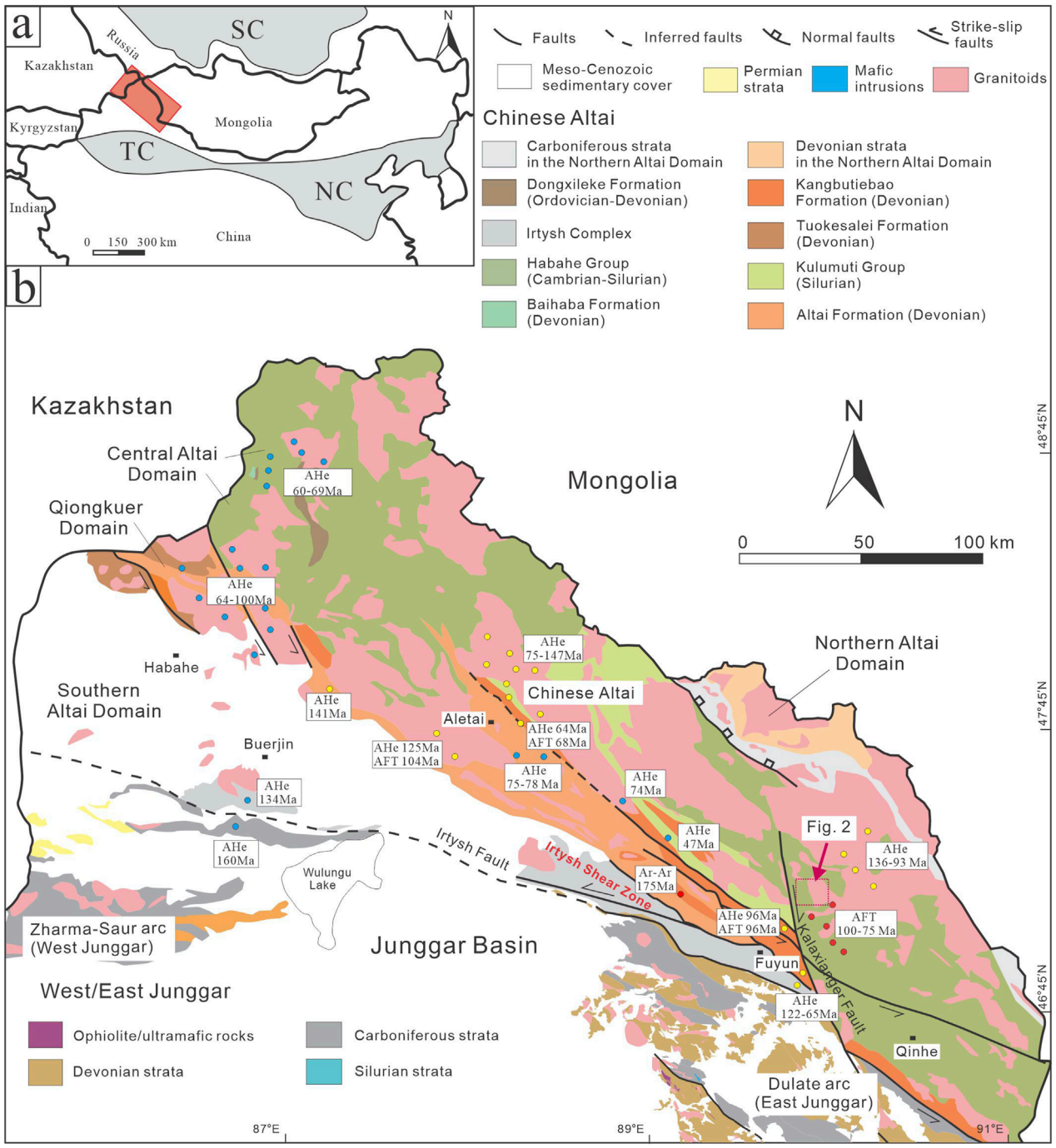

FIGURE 1
(a) Location of the Koktokay region; **(b)** geological map of the China Altai on the basis of regional 1: 200,000 geological maps (Li et al., 2019; BGMRX, 1993); and the low-temperature data are collected from Wu et al. (2023) and references therein.

west Junggar Mountains have retained the records of upper-crustal exhumation caused by Permian shortening along the Irtysh Shear Zone (Gillespie et al., 2020). The granite intrusion around the Irtysh Shear Zone recorded the intensity of deformation in different episodes. Devonian granitoids preserve deformational fabrics (Li et al., 2017; Li et al., 2022). However, Permian aged granites are commonly undeformed (Sun et al., 2008; Tong L. X. et al., 2014). The Tarim Craton collided with the Siberian Craton during the Triassic period (Xiao et al., 2009; Xiao et al., 2015; Lv et al., 2012; Zheng et al., 2015). Monazite U–Pb ages and biotite Ar–Ar cooling ages recorded in the Altai indicate exhumation of up to 20 km in relation to thrust faulting in the Late Permian to Early Jurassic (Briggs et al., 2009;

Li et al., 2015). Late in this period, numerous post-orogenic rare-metal pegmatites were formed in the Altai (Lv et al., 2012; Lv et al., 2018; Che et al., 2015; Zhou et al., 2015a; Ma et al., 2015).

The Koktokay pegmatite district is located in the middle of the China Altai (Figure 1B), where more than 3,000 pegmatites have been formed (Tang et al., 2018). These pegmatites belong to the LCT family (Černý, 1991; Černý and Ercit, 2005) and the Pegmatite family (Lv et al., 2018) based on the chemical composition–mineral assemblage–structural geology (CMS; Dill, 2016) classification with the mineralogical range of barren to Be-, Ta-, and Nb-enriched types. However, rare-metal-mineralized pegmatites account for less than 2% of the total pegmatite bodies within individual pegmatite groups (Tang et al., 2018). Within the Koktokay Pegmatite Group, the No. 3 pegmatite is the most strongly mineralized rare-metal pegmatite, containing 10 internal zones (Zou and Li, 2006).

The famous Koktokay No. 3 pegmatite is 1.5 km south of the Koktokay Town (Figure 2). Igneous rocks are widely exposed in the area. The igneous comprises a biotite batholith intruded by two-mica and muscovite granite dike (Figure 2). Zircon U–Pb dating yields ages pf 396–415 Ma for the biotite batholith (Wang et al., 2007), 390–400 Ma for the two-mica granite, and 390–396 Ma for the muscovite granite dikes (Zhou et al., 2015a). The metagabbro pluton is the host rock of the No. 3 pegmatite (Figure 2), and it was dated at 408 ± 6 by zircon U–Pb (Wang et al., 2006; Cai et al., 2012). The formation age of the No. 3 pegmatite is Late Triassic to Early Jurassic (Zircon U–Pb, Rb–Sr, and coltan U–Pb, 220–190 Ma; Wang et al., 2007; Zhou et al., 2015b; Che et al., 2015; Shen et al., 2022), and it is determined from a geochronological perspective that it has no genetic connection with the surrounding igneous rocks. Detailed geochronology studies identified that the geodynamics setting for the formation of No. 3 pegmatite is the extension stage after the collision between the Tarim Craton and Siberian Craton.

The Aler Granite is a batholith with the area exposed exceeding 1,400 km^2, located approximately 15 km north of the No. 3 pegmatite (Figure 2). This batholith extends along the trend of the Altai orogen and intrudes into the Paleozoic metasedimentary rocks (Kuwei group) and Devonian plutons. The lithology of the Aler Granite in the northern part predominantly consists of medium-fine-grained biotite granite, while in the southern part, it is predominantly porphyritic biotite granite with larger phenocrysts of quartz and feldspar (Liu et al., 2014). The primary mineral composition is quartz, K-feldspar, and biotite, while the accessory minerals include magnetite, garnet, zircon, apatite, and xenotime. According to lithology and occurrence location, the Aler Granite can be classified into central zone, transitional zone, and marginal zone (Zhang et al., 2015). Some dating methods with relatively low closure temperature had been used in the Aler Granite and revealed a younger age (e.g., biotite K-Ar 138–150 Ma and biotite $^{40}Ar/^{39}Ar$ 131.39 ± 4.25 Ma; Zhang et al., 1994; Chai et al., 2010; Han, 2008), leading to the recognition of the Aler Granite as a product of the Indosinian period. Subsequent extensive precise zircon U–Pb dating has determined its age to be Late Triassic (Liu and Han, 2019; Zhang et al., 2015; Liu et al., 2014). Nevertheless, the reported Cretaceous origin of the Aler Granite holds significance as it is correlated with the time when the Chinese Altai cooled to upper-crystal temperatures (Yuan et al., 2006; Pullen et al., 2020). It provides significant reference information for studying the preservation of the Aler Granite. Several Mesozoic granites developed in the Altai Orogenic Belt (Vladimirov et al., 2005; Annikova et al., 2006; Han, 2008), but only a few in the Chinese Altai [Jiangjunshan granite, 150 Ma, Chen and Jahn (2002); Shangkelan, 202 Ma, Wang et al. (2010); and Aler Granite, 210–219 Ma]. There is no evidence indicating that the Mesozoic Chinese Altai is not conducive to the formation of granites, so the preservation of Mesozoic granites in this area is questionable. Obviously, spherical weathering with large height differences in the Aler Granite (Liu and Han, 2019) also implies multiple stages of exhumation and denudation in this area.

2 Methods

2.1 Sample preparation

The sample locations are remarked in Figure 2. The formation of the Koktokay pegmatites is a complex process, including the initial magmatic stage, magmatic–hydrothermal transition stage, and hydrothermal stage (Zhao and Yan, 2023 and references therein). According to the occurrence of the Koktokay Pegmatite and the simulation experiment of London (2014), the graphic zone (zone I) in the external of the Koktokay No. 3 pegmatite can represent the initial pegmatitic magma. Most zircons in pegmatites are damaged by radiation due to high U and Th contents and lose their original crystal structure (Lv et al., 2018). This process turns the zircon crystals into materials filled with small pores. The destroyed crystal structure of zircon grains is not conducive to the preservation of products from multiple isotope systems (e.g., $Pb_{radiogenic}$ and He), and the fission track is even invisible. Therefore, AFT, AHe, and U–Pb ages from the No. 3 pegmatite were utilized to constrain the multistage thermal history, tracking cooling from higher to lower temperatures (Table 1). Apatite was obtained by collecting typical bulk samples from zone I (Figure 3d), followed by crushing and flotation. Then, they were divided into two groups, one for fission-track analysis (Figure 3e) and the other mounted in epoxy resin for LA-ICPMS analysis (Figure 3f).

Aler granite samples were collected from porphyritic biotite granite in the southern part of the batholith. The zircon U–Pb age and whole-rock geochemical composition are reported in Liu et al. (2012). Zircon and apatite are invisible in the porphyritic biotite granite (Figure 3a), which are obtained by crushing typical bulk rocks, flotation, and magnetic separation. Complete zircon (Figure 3b) and apatite (Figure 3c) of grains were selected for fission-track and (U–Th)/He analyses.

2.2 Apatite and zircon fission-track thermochronology

The fission-track analysis experimental works were performed at the Beijing Zekang'en Technology Co., Ltd. The obtained apatite and zircon concentrates were separated using conventional magnetic and heavy-liquid techniques. The zircon grains were mounted in glass slides, heated, and covered by FEP Teflon sheets. Their external prismatic surfaces were ground and polished. The etching duration was approximately 20–35 h with NaOH/KOH (1:1) used as the eutectic etchant at 210 °C (Garver, 2003; Yuan et al., 2007).

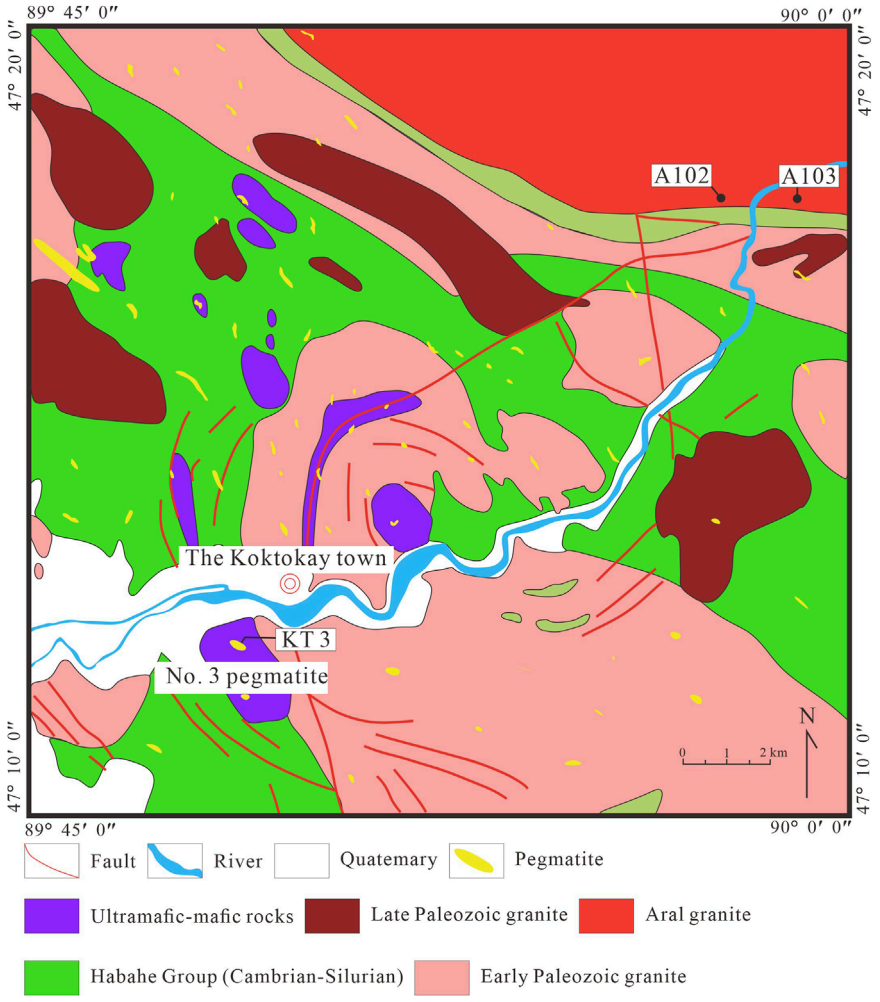

FIGURE 2
Geological map of the Koktokay area showing the distribution of the No. 3 pegmatite and the Aler granitic batholith (after Zou and Li, 2006).

Different from zircon, apatite was mounted in epoxy resin on glass slides, ground, and polished to an optical finish to expose the internal grain surface. Spontaneous tracks were revealed using 5.5 N HNO_3 for 20 s at 21 °C. Thin low-uranium muscovite used as external detectors were packed together with sample grain mounts, CN2 (apatite), and CN5 (zircon) uranium dosimeter glass (Bellemans, 1995) irradiated in the well-thermalized hot-neutron nuclear reactor (Yuan et al., 2006). After irradiation, the muscovite external detectors were detached and etched in 40% HF for 20 min at 25 °C to reveal the induced fission tracks (Yuan et al., 2003). Track densities for both natural and induced fission track populations were measured using a dry objective at ×100 magnification. Fission-track ages were measured using the IUGS-recommended zeta calibration approach. The zeta values used in this study have been determined from repeated measurements of standard apatite (Hurford and Green, 1983; Hurford, 1990). The weighted mean zeta value obtained is 391 ± 17.8 a/cm^2 for apatite and 88.2 ± 2.9 a/cm^2 for zircon.

2.3 Apatite and zircon (U–Th)/He thermochronology

Apatite and zircon (U–Th)/He analyses were conducted at the Sate Key Laboratory of Ore Deposit Geochemistry (SKLODG), Institute of Geochemistry, Chinese Academy of Sciences (IGCAS), Guiyang, China. Inclusion-free apatite and zircon grains for (U–Th)/He analysis were handpicked from concentrated separates, based on their size and euhedral crystal shape. The representative apatite and zircon grains are shown in Figure 3. The crystal size of each grain was measured microscopically for applying the alpha-ejection age corrections (Farley et al., 1996). The apatite grains were loaded into platinum capsules, and the zircon grains were loaded into niobium capsules and outgassed under vacuum at 900 °C for 5 min and 1,300 °C for 15 min. The protocols of He analysis followed the established laboratory routine extraction. The ^{4}He abundances were determined as an isotope ratio using a pure ^{3}He spike that has been calibrated against an independent ^{4}He standard (House et al.,

TABLE 1 Table of the main mid-low-temperature thermochronology tools and their closure-temperature and corresponding closure depths (after Huntington and Klepeis, 2018).

Method	Closure temperature (°C)	Closure depth (km)
Apatite (U–Th)/He	55–75	1.5–3.3
Apatite fission track	80–120	3–5.5
Zircon (U–Th)/He	160–200	5–9.5
Zircon fission track	210–300	9.7–14.5
Muscovite Ar^{40}/Ar^{39}	300–400	
Apatite U–Pb	380–600	
Zircon U–Pb	920–1,100	

2000; Wu et al., 2016). The outgassed apatite grains were dissolved with platinum capsules in 7 mol/L HNO_3 and analyzed for ^{238}U, ^{235}U, ^{232}Th, and ^{147}Sm by ICP–MS. The degassed zircon grains were transferred to Parr bombs, where they were spiked with ^{235}U and ^{230}Th and digested at 240 °C for 40 h in HF. A second bombing in HCl for 24 h at 200 °C ensured the dissolution of fluoride salts. Zircon solutions were then dried down, dissolved in HNO_3, and diluted in H_2O to 5% acidity for the analysis of ^{238}U, ^{235}U, and ^{232}Th by solution ICP–MS (Goeadow et al., 2015).

2.4 Apatite U–Pb thermochronology

Apatite U–Pb isotopic and trace element analyses were performed at the SKLODG, IGCAS, using a GeoLas Pro 193-nm excimer ArF LA system coupled with an Agilent 7500a quadrupole-based Q-ICP-MS. During Laser Ablation (LA), a National Institute of Standards and Technology (NIST) 610 SEM reference material glass was used to optimize the instrumental parameters. Using OD 306 as an external standard, the QH apatite standard [~150 Ma, Chew et al. (2016)] was used to verify the analytical accuracy and return the weighted mean $^{206}Pb/^{238}U$ age of 156 ± 4.7 Ma. NIST 612 was used for apatite trace-element calculation using Ca as the internal standard. In routine analysis, every 15 samples were followed by two runs of SEM 610, NIST 612, and OD306 and one run of Durango and QH, with a repetition of 10 Hz, a laser energy density of 3 J/cm^2, and a spot size of 60 μm. Every analysis consists of 30-s background acquisition, 60-s sample data acquisition, and approximately 60-s blank for flashing. The fractionation correction and U–Pb ages were calculated using GLITTER 4.0 (GEMOC, Macquarie University). The Concordia and weighted mean U–Pb age were calculated using the ISOPLPT/EX 4.15 software package.

2.5 Thermal history modeling

The cooling histories of the pegmatite and granite (KT3, A102, and A103) were derived using the HeFTy program (v 2.0.0; Ketcham et al., 2007). The dominant input data are apatite fission-track spontaneous and induced track densities, length–frequency distributions, and kinetic parameters D_{par}. Monte Carlo simulation was used in modeling operation. The model was constrained at the start by the ages and closure temperatures of apatite U–Pb and ZFT in the Koktokay No. 3 pegmatite and the Aler Granite, respectively. We used the multi-kinetic fission-track annealing model of Ketcham et al. (2007), and the initial track length in apatite was set as 16.3 μm (Ketcham, 2005). Available AHe and ZHe data were integrated using the radiation damage accumulation and annealing, with helium diffusion models (Flowers et al., 2009; Gautheron et al., 2013). The present-day surface temperature is constrained at 20 °C ± 10 °C.

3 Results

3.1 Fission-track analysis

3.1.1 AFT data

Apatite fission-track dating was performed on samples KT3, A102, and A103. The detailed results are shown in Table 2. For every sample, the central age is calculated based on 35 grains in KT3 and 42 grains in A102 and A103. The samples A102 and A103 passed the χ^2 test [P(χ^2)-values are 12% and 11.3%, respectively], indicating a relatively concentrated age of single particles. Their central ages were determined to be 60.69 ± 8.08 Ma (Figure 4b) and 48.13 ± 5.73 Ma (Figure 4c), respectively. Although the sample KT3 did not pass the χ^2 test, the dispersion value is 11.8% ± 5.2%, indicating a relatively discrete age of single particles. It may be caused by the high content of U in pegmatitic apatite (Glorie et al., 2023; McDannell, 2020). The pooled age was used to replace the central age in KT3, and its pooled age is 68.78 ± 7.22 Ma (Figure 4a). Mean track lengths of the three samples vary between 11.29 and 13.08 μm (Table 2). They are relatively short confined track lengths, suggesting more intensive thermal annealing. The average etch diameter (D_{par}) values of the samples range from 1.426 to 1.714 μm, which were shorter than those of the Durango apatite (~1.75 μm), indicating relatively weaker resistance to fission-track annealing (Donelick et al., 2005).

3.1.2 ZFT data

The zircons from the Aler Granite were analyzed using ZFT (samples A102 and A103). Both of their ZFT ages passed the χ^2 test (Table 2). Their central ages are 150.73 ± 11.56 Ma (Figure 4d) in A102 and 145.89 ± 8.52 Ma (Figure 4e) in A103. ZFT analysis predominantly focused on density measurement owing to the lack of unified standards, while the neglected track length analysis would be a significant parameter for evaluating the thermal histories. All the tracks in zircon have the same initial track length (~10 μm; Tagami et al., 1998). Thus, we selected the classical standard of Garver (2003) and obtained the mean track lengths of 9.97 and 9.88 μm in A102 and A103, respectively (Table 2). The track length in zircon is nearly initial, indicating that the obtained tracks did not suffer annealing and that the two concentrated ages of ZFT have not been reset.

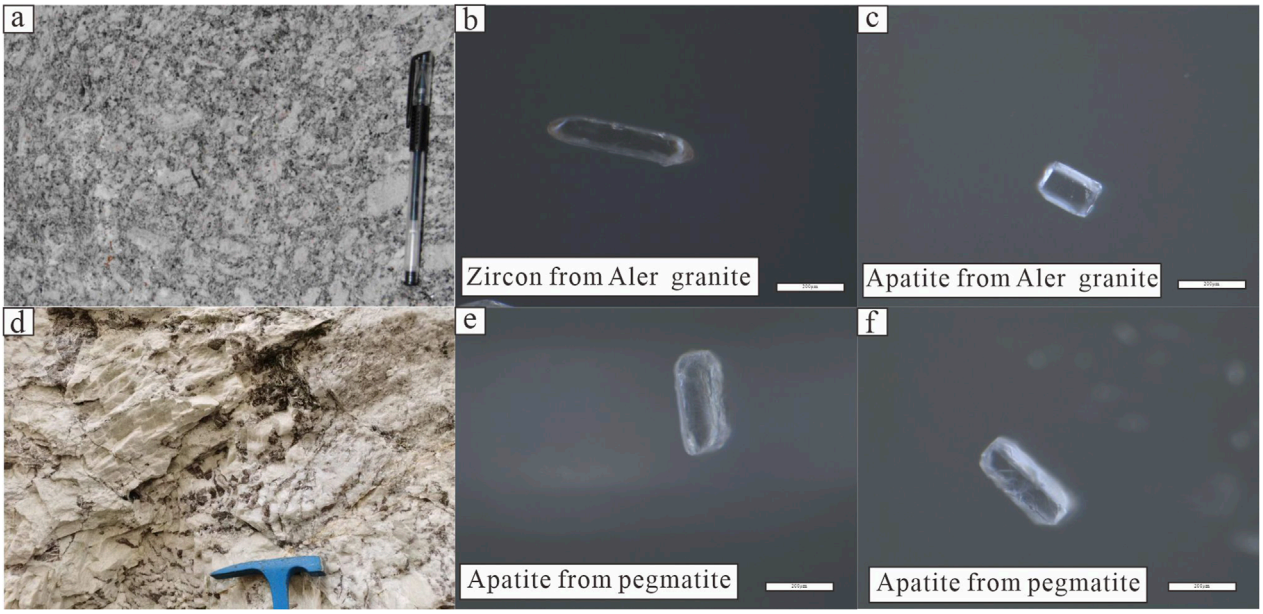

FIGURE 3
Sampled porphyritic biotite granite **(a)**, with obtained zircon **(b)** and apatite **(c)** grains; sampled graphic pegmatite **(d)**, and obtained apatite **(e,f)**.

TABLE 2 Apatite and zircon fission-track results.

Analytical methods	Sample no.	Location	No. of grains	N_s	ρ_s (10^5/ cm^{-2})	N_i	ρ_i (10^5/ cm^{-2})	^{238}U (ppm)	D_{par} (μm)	P (χ^2) (%)	Central age (Ma, 1 σ)	N_{length}	Mean track length (μm)
AFT	KT3	Graphic zone in the No. 3 pegmatite	35	3,440	17.833	12,560	65.111	61.4	1.426	1.3×10^{-3}	68.78 ± 7.22 (Pooled age)	194	13.08
	A102	Southern part of Aral granite	42	663	2.58	2,369	9.222	10	1.54	12	60.69 ± 8.08	153	11.33
	A103	Southern part of Aral granite	42	1,087	4.604	5,030	21.305	23.7	1.714	11	48.13 ± 5.73	164	11.29
ZTF	A102	Southern part of Aral granite	34	5,652	188.4	2,381	79.367	205.6	-	7.3	150.1 ± 12.9	139	9.97
	A103	Southern part of Aral granite	26	3,775	156.639	1701	70.581	168.6	-	5.3	154.1 ± 14.8	173	9.87

Note: Ns (ρ_s) and Ni (ρ_i) are the number (density) of counted spontaneous and induced tracks in the external detector, respectively; P (χ^2) is the probability of obtaining a χ^2 value for v degrees of freedom, where v = no. of crystals − 1; D_{par} is the long axis of the track etch pit; N_{length} is the number of lengths measured.

3.2 (U–Th)/He analysis

Apatite helium ages were measured on pegmatite and granite (samples KT3 and A102), and zircon helium ages were measured on granite (samples A102 and A103); all results are shown in Table 3. The obtained datasets of pegmatite and granite samples show a low degree of single-grain helium age dispersion. Five apatite grains from the pegmatite sample KT3 yielded a weighted mean AHe age of 83.9 ± 4.5 Ma, and three grains from the sample A102 yielded an age of 56.5 ± 3.2 Ma. Meanwhile, five zircon grains of the sample A102 and five zircon grains of A103 produced mean ZHe ages of 65.1 ± 3.3 Ma and 64.8 ± 3.3 Ma, respectively. Comparison between (U–Th)/He and fission-track ages within a single sample shows that dating methods involving a higher isotope closure temperature

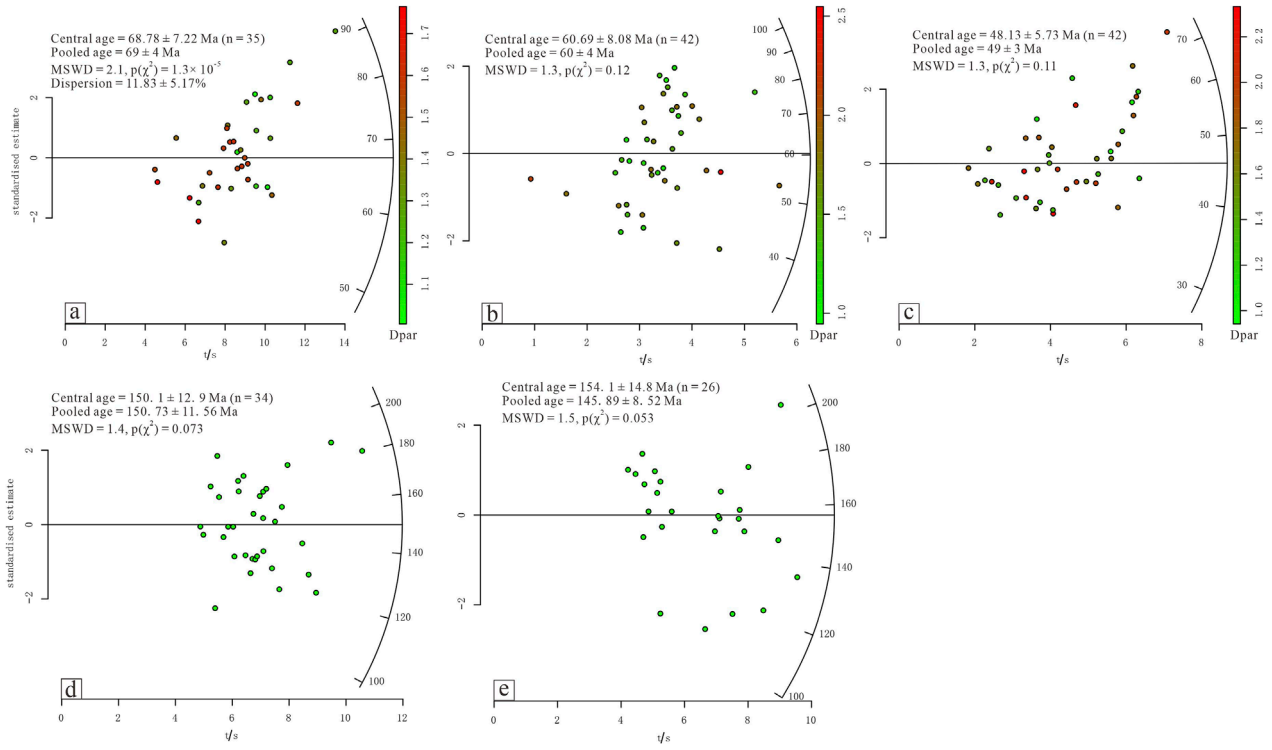

FIGURE 4
Radial plots of apatite FT **(a–c)** and zircon FT **(d,e)** ages using the Radialplotter (Vermeesch, 2009).

generally display older corresponding ages. Moreover, all of them are significantly younger than the Koktokay Pegmatite and Aler Granite formation (~220 Ma; Wang et al., 2007; Liu et al., 2014).

3.3 Apatite U–Pb data

The apatite grains of KT3 selected for U–Pb dating are shown in Figure 5a. The analytical spots yielded a Tera-Wasserburg U–Pb lower intercept age of 176 ± 11 Ma (n = 14, MSWD = 0.41, Figure 5b).

The trace element content of apatite is shown in Table 4. The apatite Rare Earth Elements (REE) content ranges from 300 to 600 ppm, which is consistent with previous investigations (Zhang, 2001; Cao et al., 2013) and is different from apatite of other zones in No. 3 pegmatite. In addition, the chondrite-normalized REE patterns of apatite have obvious negative Eu anomalies, with Eu/Eu*ratios of 0.16–0.04. According to Masuda et al. (1994) and Irber (1999), the provided quantitative method is used to describe the REE distribution characteristic (Table 4; Figure 5c). The t_1, t_3, and t_4 values of all apatite are >1.1, and t_3>t_4>t_1, which indicates that the "quadruple effect" of apatite is most developed in the third segment (Gd-Ho). All values of $t_{3,4}$ and $t_{1,3,4}$ > 1.5, implying that the apatite analyzed have a significant M-type tetrad effect. This is consistent with the REE distribution features of minerals in the external zones in No. 3 pegmatite (Cao et al., 2013; Zhang, 2001). Therefore, the analyzed apatite crystallized during the pegmatitic magma stage.

3.4 Thermal history modeling results

All three samples (KT3, A102, and A103) in this study obtained acceptable [GOF (good of fit) > 0.3] or good (GOF >0.7) thermal modeling results. Inverse thermal history models are detailed in Figures 6–8. All the three samples show observed similar cooling paths (i.e., the best-fit path). They entered the ZHe PRZ in the Early Cretaceous, followed by prolonged slow cooling since the Middle Cretaceous. All three samples display a complex three-stage cooling, and a change in the cooling rate (to a slower rate) can be observed in the Cretaceous (~120 Ma). The modeling shows an accelerated cooling between ~170 and 120 Ma, with a cooling rate of >3 °C/Ma, and subsequent moderate cooling between ~120 and 60 Ma, with a cooling rate of ~1.5 °C/Ma, followed by a slow cooling rate of <0.5 °C/Ma until the present. Cooling rates of <~0.5 °C/Ma, ~0.5 °C–2.0 °C/Ma, and >~2.0 °C/Ma are defined as slow, moderate, and rapid, respectively, in an intracontinental setting (based on empirical values, Wu et al., 2023; He et al., 2022).

4 Discussion

4.1 Cooling history of the Koktokay district

The previous studies on the uplift of high-elevation low-relief surfaces in the China Altai proposed a rapid cooling in the Cretaceous (Yuan et al., 2006; Jolivet et al., 2007; Vassallo et al., 2007; Pullen et al., 2020). Our results from the

10.3389/feart.2025.1573046

TABLE 3 Apatite and zircon (U–Th)/He results.

Sample	Length (μm)	Width1 (μm)	Width2 (μm)	Radius (μm)	FT	^{238}U (mol)	Std.^{238}U (mol)	^{232}Th (mol)	Std.^{232}Th (mol)	^{4}He (mol)	Std. ^{4}He (mol)	Th/U	Age (Ma)	Cor. Age (Ma)	±1σ (Ma)
KT3 (Apatite)															
Kt3-a1	270	83	81	53	0.71	1.35×10^{-15}	3.71×10^{-16}	7.69×10^{-15}	5.06×10^{-16}	2.37×10^{-16}	3.64×10^{-18}	5.71	58.98	82.70	10.33
Kt3-a3	316	147	102	78	0.81	9.07×10^{-14}	5.38×10^{-15}	3.73×10^{-14}	1.46×10^{-15}	9.40×10^{-15}	1.13×10^{-16}	0.41	73.43	90.78	5.02
Kt3-a4	309	146	109	79	0.86	1.29×10^{-13}	7.58×10^{-15}	4.27×10^{-14}	1.58×10^{-15}	1.33×10^{-14}	1.60×10^{-16}	0.33	73.99	85.61	4.76
Kt3-a5	411	175	166	106	0.92	1.71×10^{-13}	1.01×10^{-14}	6.92×10^{-14}	2.17×10^{-15}	1.68×10^{-14}	2.03×10^{-16}	0.40	69.64	75.90	4.14
Kt3-a9	307	170	158	97	0.85	1.95×10^{-13}	1.13×10^{-14}	8.21×10^{-14}	1.50×10^{-15}	2.03×10^{-14}	2.58×10^{-16}	0.42	73.59	86.52	4.69
A102 (Apatite)															
A2-4	356	112	103	70	0.78	6.30×10^{-14}	3.80×10^{-15}	1.67×10^{-13}	4.41×10^{-15}	6.10×10^{-15}	7.68×10^{-17}	2.65	46.68	59.59	2.43
A-11	159	117	88	58	0.74	1.73×10^{-14}	1.19×10^{-15}	2.08×10^{-14}	6.47×10^{-16}	1.10×10^{-15}	1.51×10^{-17}	1.20	38.75	52.41	2.91
A-5	263	127	97	69	0.78	1.02×10^{-13}	5.98×10^{-15}	6.31×10^{-15}	4.92×10^{-16}	5.80×10^{-15}	7.65×10^{-17}	0.06	43.63	55.88	3.30
A102 (Zircon)															
Z-6	346	133	112	78	0.84	1.03×10^{-11}	5.88×10^{-13}	1.55×10^{-12}	2.36×10^{-14}	7.40×10^{-13}	9.07×10^{-15}	0.15	53.84	64.17	3.60
Z-7	177	86	62	46	0.73	2.62×10^{-12}	1.49×10^{-13}	6.78×10^{-13}	1.05×10^{-14}	1.56×10^{-13}	1.93×10^{-15}	0.26	43.75	60.21	3.31
Z-8	177	94	87	54	0.77	4.21×10^{-12}	2.40×10^{-13}	8.13×10^{-13}	1.25×10^{-14}	3.33×10^{-13}	4.15×10^{-15}	0.19	58.92	76.72	4.27
Z-10	251	117	108	69	0.82	5.48×10^{-12}	3.12×10^{-13}	9.99×10^{-13}	1.53×10^{-14}	4.42×10^{-13}	5.62×10^{-15}	0.18	60.10	73.50	4.11
Z-11	356	99	85	61	0.79	7.04×10^{-12}	4.01×10^{-13}	1.26×10^{-12}	1.93×10^{-14}	4.39×10^{-13}	5.58×10^{-15}	0.18	46.48	58.52	3.27

(Continued on the following page)

TABLE 3 (*Continued*) Apatite and zircon (U–Th)/He results.

Sample	Length (μm)	Width1 (μm)	Width2 (μm)	Radius (μm)	FT	^{238}U (mol)	Std.^{238}U (mol)	^{232}Th (mol)	Std.^{232}Th (mol)	^{4}He (mol)	Std. ^{4}He (mol)	Th/U	Age (Ma)	Cor. Age (Ma)	±1σ (Ma)
A103 (Zircon)															
Z-1	376	84	77	55	0.77	7.91 × 10^{-12}	4.51 × 10^{-13}	1.18 × 10^{-12}	1.81 × 10^{-14}	5.58 × 10^{-13}	7.11 × 10^{-15}	0.15	52.90	68.71	3.87
Z-2	440	103	86	64	0.80	1.56 × 10^{-11}	8.89 × 10^{-13}	3.48×10^{-12}	5.27×10^{-14}	1.41 × 10^{-12}	1.81 × 10^{-14}	0.22	66.68	82.96	4.59
Z-3	277	103	83	60	0.79	4.55 × 10^{-12}	2.59 × 10^{-13}	1.49 × 10^{-12}	2.27 × 10^{-14}	3.45 × 10^{-13}	4.44 × 10^{-15}	0.33	54.75	69.32	3.76
Z-4	185	86	60	46	0.89	3.29 × 10^{-12}	1.88 × 10^{-13}	2.73 × 10^{-13}	4.35 × 10^{-15}	1.99 × 10^{-13}	2.54 × 10^{-15}	0.08	46.18	52.06	2.98
Z-5	243	116	107	68	0.82	4.86 × 10^{-12}	2.77 × 10^{-13}	9.27 × 10^{-13}	1.42 × 10^{-14}	3.44 × 10^{-13}	4.38 × 10^{-18}	0.19	52.66	64.60	3.61

Note: FT is the ejection correction after Farley et al., 1996.

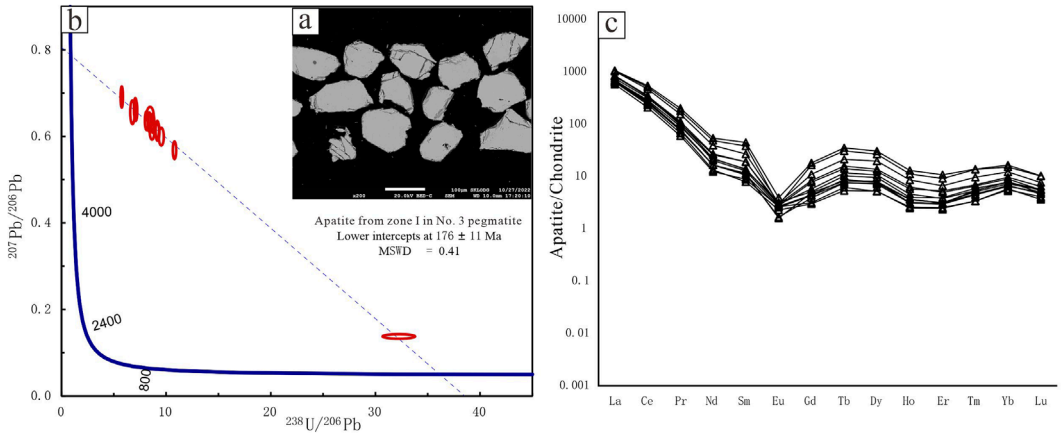

FIGURE 5
Back-scattered electron (BSE) images of the KT3 apatite grains for U–Pb dating **(a)**; Tera–Wasserburg diagram for apatite U–Pb dating **(b)**; and the chondrite-normalized REE pattern **(c)**.

Koktokay No. 3 pegmatite and Aler Granite show a history of relative intact cooling/exhumation, roughly consistent with those of the whole China Altai, which shed light on the preservation of rare-metal pegmatite groups. Given the exhumation scenarios of the Koktokay, we further provide constraints on the preservation of the rare-metal pegmatite ore deposit and discuss the potential of pegmatite-type rare-metal mineral exploration in the Koktokay region.

4.1.1 Middle Jurassic to Cretaceous (~170–120 Ma) rapid cooling of Koktokay

As described above, a significant cooling phase in the Mesozoic in Koktokay district is recorded by the thermal history modeling of our pegmatite and granite samples. This phase of the cooling prevails within the whole Altai, and numerous studies have even documented consistent low-temperature cooling ages from eastern Kazakhstan to Lake Baikal in south-eastern Siberia in the Mesozoic (Glorie et al., 2023; Glorie and De Grave, 2016; McDannell et al., 2018; Glorie et al., 2012; Vassallo et al., 2007). Previous low-temperature thermochronology studies in the Altai shows that different Early Jurassic and Cretaceous AFT ages were obtained from the Mongolia Altai (McDannell et al., 2018; Jolivet et al., 2007; Vassallo et al., 2007). Siberia Altai-Sayan also experienced a rapid cooling phase in the Jurassic period (Glorie et al., 2012). The apatite fission-track thermochronology revealed a cooling phase in the Late

TABLE 4 The REE contents of apatite.

Sample	La	Ce	Pr	Nd	Sm	Eu	Gd	Tb	Dy	Ho	Er	Tm	Yb	Lu	t_1	t_3	t_4	$t_{3,4}$	$t_{1,3,4}$
KTA-1	146	143	6.47	6.37	1.44	0.173	0.655	0.266	1.59	0.15	0.387	0.102	0.904	0.099	1.38	2.29	1.53	1.87	2.2
KTA-2	195	212	10.7	12.7	2.9	0.173	1.71	0.593	3.49	0.358	0.821	0.168	1.53	0.14	1.32	2.03	1.47	1.73	1.98
KTA-3	137	129	5.72	5.8	1.36	0.154	0.648	0.231	1.32	0.148	0.422	0.086	0.949	0.104	1.33	1.97	1.35	1.63	1.88
KTA-4	167	169	7.6	7.78	1.64	0.149	0.884	0.289	1.83	0.176	0.49	0.114	1.1	0.127	1.37	2.04	1.4	1.69	1.98
KTA-5	160	162	7.49	7.73	1.67	0.098	0.799	0.283	1.9	0.205	0.523	0.13	1.24	0.141	1.37	2	1.45	1.7	1.99
KTA-6	155	157	7.21	7.78	1.76	0.093	1	0.308	2.04	0.208	0.516	0.118	1.15	0.119	1.33	1.92	1.46	1.68	1.94
KTA-7	253	334	19.2	25.5	6.86	0.229	3.75	1.32	7.77	0.737	1.78	0.352	2.8	0.262	1.38	2.13	1.43	1.74	2.05
KTA-8	249	314	17.2	22.9	5.82	0.166	3.39	1.15	6.77	0.631	1.52	0.347	2.58	0.258	1.34	2.11	1.49	1.77	2.05
KTA-9	202	215	10	10.4	2.08	0.187	1.05	0.383	2.45	0.225	0.651	0.152	1.32	0.145	1.4	2.21	1.44	1.78	2.1
KTA-10	180	195	9.81	12.2	2.92	0.159	1.6	0.53	3.17	0.329	0.877	0.177	1.65	0.164	1.29	1.98	1.4	1.67	1.89
KTA-11	244	288	14.8	18.4	4.12	0.181	2.26	0.798	5.01	0.488	1.1	0.247	2.08	0.194	1.35	2.11	1.53	1.79	2.08
KTA-13	200	205	9.21	9.47	1.95	0.156	0.915	0.328	1.97	0.18	0.51	0.138	1.33	0.139	1.37	2.19	1.58	1.86	2.18
KTA-13	161	177	8.62	10.1	2.14	0.17	1.19	0.44	2.73	0.26	0.63	0.137	1.34	0.124	1.33	2.18	1.51	1.82	2.1
KTA-14	151	147	6.44	6.25	1.22	0.133	0.618	0.202	1.34	0.141	0.411	0.087	0.985	0.093	1.38	1.95	1.47	1.69	1.99

Element concentrations are in ppm, where t1 = (Ce*Pr/La*Nd)cn0.5; t2 = (Tb*Dy/Gd*Ho)cn0.5; t4 = (Tm*Yb/Er*Lu)cn0.5; t3,4 = (t3*t4)0.5; t1,3,4 = (t1*t3*t4)0.5. The subscript "cn" denotes chondrite-normalized values. The rare earth element tetrad-effect method is described by Irber (1999).

10.3389/feart.2025.1573046

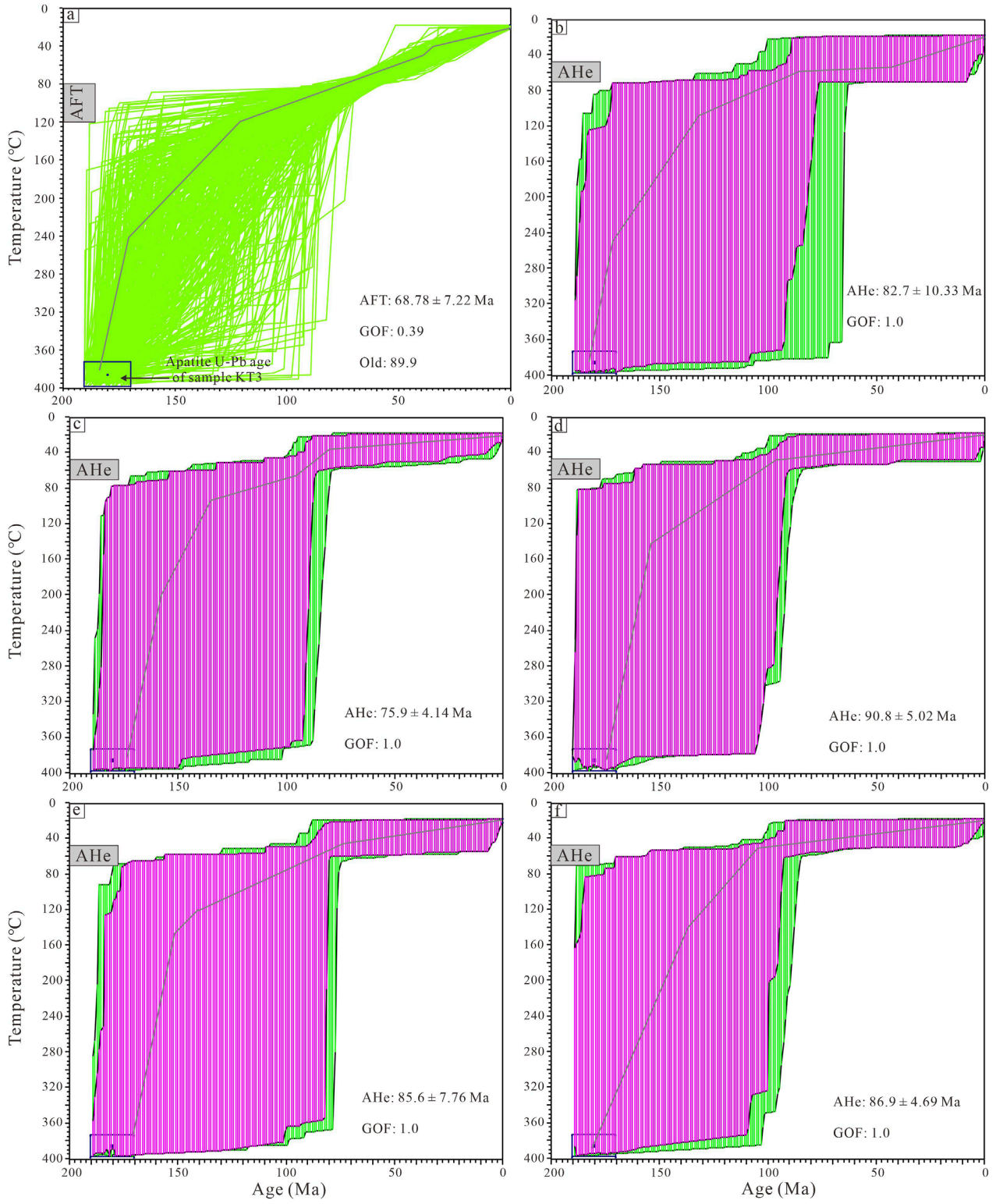

FIGURE 6
Results of HeFTy thermal history modeling of the sample KT3 from the No. 3 pegmatite. Green and purple colors show accept-fit solutions (goodness of fit >5%) and good-fit solutions (goodness of fit >50%), respectively; the rectangular boxes represent the time–temperature constraints; the best-fit path is plotted with a black curve. **(a)** AFT: Apatite fission track; **(b–f)** AHe: Apatite (U-Th)/He; GOF: good of fit; Old: The age (Ma) of the oldest fission track that has not yet been fully annealed.

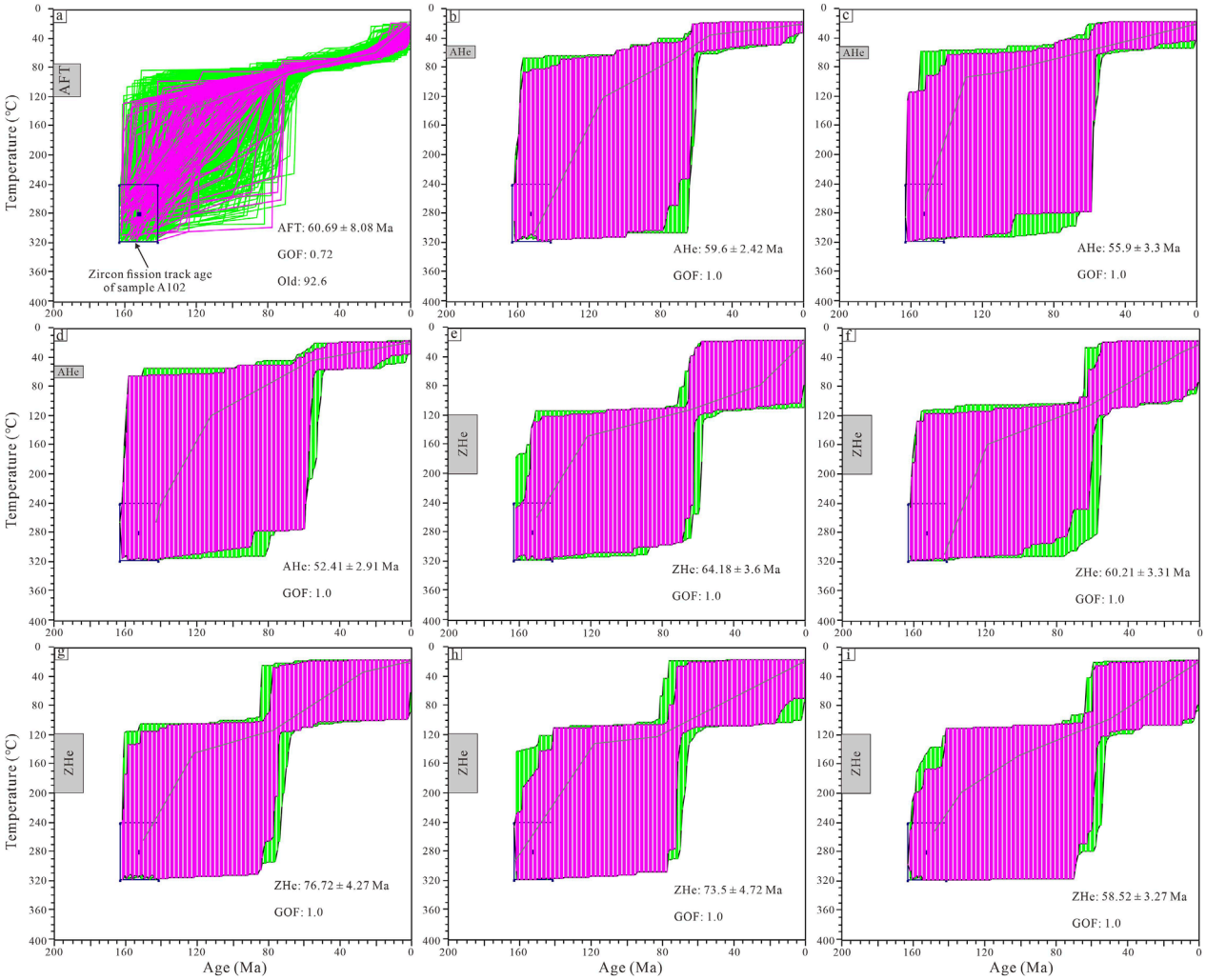

FIGURE 7
Results of HeFTy thermal history modeling of the sample A102 from the Aler granitic batholith. Green and purple colors show accept-fit solutions (goodness of fit >5%) and good-fit solutions (goodness of fit >50%), respectively; the rectangular boxes represent the time–temperature constraints; the best-fit path is plotted with a black curve. **(a)** AFT: Apatite fission track; **(b–d)** AHe: Apatite (U-Th)/He; **(e–i)** ZHe: zircon (U-Th)/He; GOF: good of fit; Old: The age (Ma) of the oldest fission track that has not yet been fully annealed.

Jurassic–Cretaceous (De Grave et al., 2013; Guenthner et al., 2013). All these results investigated from the Altai and adjacent regions imply that this area experienced accelerated cooling during the Mesozoic, while the exhumation process differs spatiotemporally (Wu et al., 2023).

In the Early Mesozoic, there were active intracontinental fault movements in the China Altai. The intracontinental A-type subduction and obduction nappe were associated with strong magmatic activities. A biotite $^{40}Ar/^{39}Ar$ plateau age of 186 Ma was obtained for the Kangbutiebao granite, and a whole-rock Rb–Sr isochrone age of 172.8 Ma was determined for the Aweitan two-mica granite (Hu et al., 2000). These ages reflect tectonic–magmatic mineralization in 170–120 Ma, corresponding to the Cretaceous or late Yanshan period, consistent with the Aler Granite ages of 150.1 ± 12.9 Ma (Figure 4d) and 154.1 ± 14.8 Ma (Figure 4e) from ZFT ages and the Koktokay No. 3 pegmatite of 176 ± 11 Ma from apatite U–Pb age (Figure 5b). Moreover, the muscovite granite and altered biotite granite in Koktokay district also reported $^{40}Ar/^{39}Ar$ plateau ages of 181 Ma and 177 Ma, respectively (Shen et al., 2022). The Early Mesozoic ages of these geobodies are all derived from dating methods using moderate closure temperatures (<350 °C). It indicates that Koktokay district, even the middle Altai, cooled to a moderate temperature range until the Early Mesozoic. Actually, during the formation of the Koktokay Pegmatite Group and the Aler Granite (~220–210 Ma), the region experienced the end stage of Permian–Triassic high-temperature retrograde metamorphism (Tong et al., 2013; Tong Y. et al., 2014) and the onset of extensive hydrothermal events (Glorie et al., 2023; Zhou et al., 2015a). This makes it exceptionally difficult to constrain the preservation of pegmatite from magma consolidation to the Late Cretaceous period. The rapid cooling rate of >3.0 °C/Ma between approximately 170 and 120 Ma (Figure 6) would be caused at least by the combined effect of the following reasons: 1) in response to the large-scale cooling event of the Mesozoic Altai, which was inferred to be a

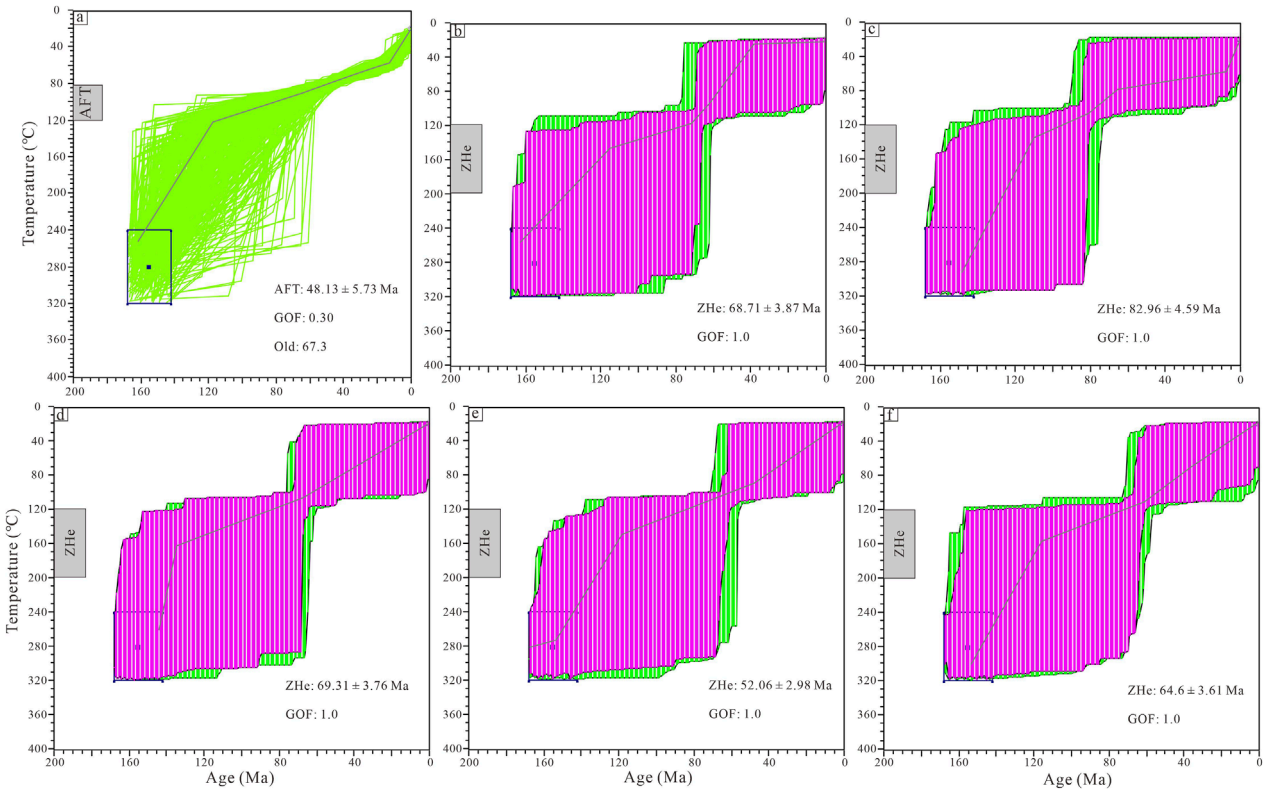

FIGURE 8
Results of HeFTy thermal history modeling of the sample A103 from the Aler granitic batholith. Green and purple colors show accept-fit solutions (goodness of fit >5%) and good-fit solutions (goodness of fit >50%), respectively; the rectangular boxes represent the time–temperature constraints; the best-fit path is plotted with a black curve. **(a)** AFT: Apatite fission track; **(b–f)** ZHe: zircon (U–Th)/He; GOF: good of fit; Old: The age (Ma) of the oldest fission track that has not yet been fully annealed.

distant effect from the North China–Eurasia collision (Buslov, 2011; De Grave and Buslov, 2007) or closure of the Mongolo–Okhotsk Ocean (Zorin, 1999); 2) a relatively high temperature (>350 °C) had been maintained by the extensive hydrothermal events in Koktokay district (stated at ~170 Ma; Glorie et al., 2023; Zhou et al., 2015b). This event had contributed to the mineralization of hydrothermal deposits such as Au–Cu–Pb–Zn (Liu et al., 2014; Zheng et al., 2017). Meanwhile, it ceased at the latest at ~150 Ma recorded by granite apatite U–Pb (Zhou et al., 2015b). Subsequently, the temperature rapidly cooled down; 3) the crystallization and cooling processes of pegmatitic melt are controversial. One speculation is that the internal temperature of pegmatite remained above the liquidus line until the Jurassic. The thermal relaxation or cooling of the rock mass itself may also contribute to the Early Jurassic apatite U–Pb age of the pegmatite sample. Both reasons 1) and 2) are not conductive to the preservation of rare-metal pegmatite, especially reason 2), where extensive hydrothermal activity is destructive to the active element ore such as Li–Rb–Cs ore. Therefore, the stage ranging from Middle Jurassic to Early Cretaceous is not conducive to the preservation of Koktokay rare-metal pegmatites and may even damage the deposit to a certain extent.

4.1.2 Middle to Late Cretaceous (~120–66 Ma) moderate rate of exhumation

As shown in Figure 9, a cooling/exhumation episode since the Middle to Late Cretaceous, which is also a widespread cooling event in the China Altai, is recorded in our samples. The cooling rates we obtained are more consistent with those reported in previous studies, rather than the extremely rapid cooling rates of the Early Cretaceous. It indicates complete consolidation of the pegmatite without regional hydrothermal activity. Notably, by summarizing the low-temperature thermochronological data on the whole Altai in the Mesozoic (Glorie et al., 2023), it was found that, at higher elevations (>1,500 m), such as the middle-northern China Altai and Siberia Altai, AFT data showed concentrated ages with narrow fission-track distributions (De Grave et al., 2008; De Grave et al., 2009; Jolivet et al., 2007; Yuan et al., 2006), suggesting rapid cooling rates. Meanwhile, a range of apparent AFT ages and AHe age of pegmatite (>75 Ma) can be observed in moderate topographic relief of Koktokay, reflective of slow cooling at low elevations (<1,500 m). As these rapid Late Cretaceous cooling ages are preserved at high altitude, it indicates that a younger, secondary exhumation event was limited to preserve the Late Cretaceous AFT ages.

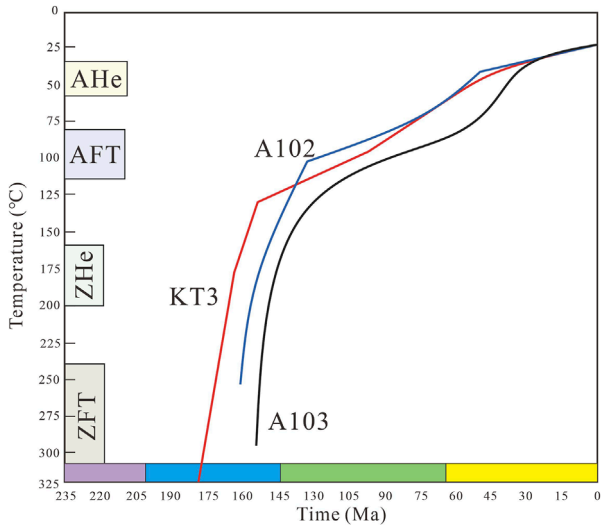

FIGURE 9
Interpreted thermal history of the Koktokay Pegmatite Group generated in the HeFTy modeling. It is derived from the weighted average path of each sample.

Furthermore, for Koktokay district located in the east of the Kalaxianger Fault, contrasting AFT data are evident on either side of the Kalaxianger Fault (Figure 1). The Kalaxianger dextral transpressional fault is the largest NNW–SSE fault in the China Altai. The average strike of this NE dipping fault is 165° with a dip angle of 65°–85° (Fu et al., 2010). K–Ar (~276 Ma) and ^{40}Ar–^{39}Ar (~282 Ma) ages from an associated pseudotachylite indicate that the earliest movement of this fault can be traced back to at least the Permian (Briggs et al., 2009). The samples taken to the east of the Kalaxianger Fault recorded rapid Late Cretaceous exhumation, while samples to the west did not. Away from the WNW–ESE-striking faults associated with the Irtysh Shear Zone, Late Jurassic–Early Cretaceous thermal processes underwent gradual cooling. The differential factor of AFT ages and cooling with respect to the Kalaxianger Fault is observed in the Late Mesozoic as samples from the more uplifted west of the fault preserved shorter apatite mean fission track lengths (<13 μm; Glorie et al., 2023), suggesting preservation of a single substantive cooling event in the Late Cretaceous, as opposed to a mixed uplift history including later differential uplift during the Cenozoic (Fu et al., 2010; Yuan et al., 2006). Therefore, it is considered that the Kalaxianger Fault was active during the Late Cretaceous (Glorie et al., 2023). Due to the differential uplift, topography preserved to the west of the Kalaxianger Fault is lower than that to the east, which, to some extent, caused erosion and exhumation of shallow pegmatite in the Koktokay district. Late Cretaceous exhumation is coeval with a series of far-field tectonic events, although the precise cause of reactivation within the Altai remains unclear. This exhumation coincided with the collapse of the Mongol–Okhotsk Orogen to the east and slab rollback in the Tethys Ocean to the south, both occurring approximately 100–80 Ma (Yin et al., 2019; Glorie et al., 2019; Ma et al., 2013; Metelkin et al., 2012; Dilek and Furnes, 2009; Jolivet et al., 2009). These events are potential drivers of stress propagation into the continental interior, leading to reactivation and exhumation. However, the current data do not clarify the extent to which these factors influenced reactivation within the Altai.

4.1.3 Cenozoic slow exhumation process

Following the Mesozoic, there was a slow and slight exhumation in the studied area (Figure 9). Many scholars consider that much of the modern topography was formed in response to deformation caused by the India–Asia collision (Molnar and Tapponnier, 1975; Sobel et al., 2006). The Altai Mountains experienced enhanced stress caused by the India–Asia collision, which reactivated preexisting basement structures and led to extensive uplift (Yuan et al., 2006; Jolivet et al., 2007; Vassallo et al., 2007). Moreover, the Cenozoic deformation and stable isotope evidence also support surface uplift since the early Oligocene (Caves et al., 2017; Caves et al., 2014; De Grave and Buslov, 2007). However, on the one hand, the low elevation (<1,500 m) of the China Altai orogenic belt is relative to other ranges of whole Altai. The majority of pre-Mesozoic basement rocks in Altai, and even across Central Asia, show evidence of Mesozoic low-temperature thermochronology, whereas Cenozoic rapid cooling and exhumation are observed only in very localized regions with high elevation (Wu et al., 2023; He et al., 2022; Gillespie et al., 2021; Jepson et al., 2018; Wang et al., 2007). On the other hand, crustal deformation alone is not a sufficient and necessary condition for driving exhumation, and the topographic and denudational evolution of orogenic belts are also strongly coupled with climate (Jepson et al., 2021; Pullen et al., 2020). Aridity has been connected to mountain building in CAOB since the Late Cretaceous (Jepson et al., 2021), which was also marked by the sedimentary records in the adjacent Junggar basin. Since the Late Cretaceous, the Junggar basin has been affected by global climate cooling and uplift of the Tibetan plateau, and the degree of dryness has been continuously intensified (Wang et al., 2019). On the contrary, during the Late Triassic to Early Jurassic, humidity is thought to have reached a maximum in the Junggar basin and adjust area, as evidenced by the retrogradation of deltaic and fluvial facies and the expansion of deep-water facies (Yang et al., 2015). The recorded humid climate coincided with the large-scale Mesozoic exhumation in the Koktokay area, while the arid climate limited denudation during the Cenozoic. The earliest Paleogene ages of (U–Th)/He in this study also contribute to minimal denudation in the China Altai since the Late Cretaceous (Caves et al., 2014; Caves et al., 2017), which is conductive to the preservation of the Koktokay Pegmatite Group.

4.2 Estimation of Koktokay rare-metal pegmatite group exhumation

The uplift and exhumation history of deposit is significant evidence to estimate the potential for further deep exploration. Thermal history modeling has been used to estimate the exhumation rates and erosion thickness of the Koktokay Pegmatite Group. Although the Koktokay Pegmatite apatite U–Pb age limits the rapid cooling since the Late Jurassic (~176 Ma; Figure 5a), the ^{40}Ar/^{39}Ar plateau ages of muscovite granite and altered biotite granite in the Koktokay area support this onset of cooling (181 Ma and 177 Ma, respectively; Shen et al., 2022). The recorded ages of the above dating

tools, with closure temperatures of ~400 °C, probably fall within a delicate evolutionary range of the fluid stage before complete crystallization of pegmatite (Thomas and Davidson, 2015; London, 2018). In addition, the Early Jurassic extensive hydrothermal event in Koktokay (Glorie et al., 2023; Zhou et al., 2015b) interfered with the calculation of exhumation in this stage. Therefore, we here calculate exhumation rates since ~150 Ma with constraints by ZFT ages (Figures 4d,e).

The constant geothermal gradient is assumed to be 30 °C ± 2 °C/km. We utilized various low-temperature geochronological tools to reconstruct the thermal history of the Koktokay Pegmatite Group area, and the predominant exhumation stage in the Cretaceous has been identified. Based on the obtained thermal history paths (Figure 9), we estimated the maximum and minimum temperature changes of each stage, divided by the assumed geothermal gradient, to derive the exhumation thickness. Subsequently, we divided the exhumation thickness by the duration of rapid uplift to estimate the rate. The results indicate a temperature change of ~110 °C ± 20 °C, an exhumation thickness of 3.6 ± 0.65 km, and an exhumation rate of 0.046 ± 0.008 km/Ma during the Cretaceous. After this time, there is a final significant cooling stage between the Paleocene and the Eocene, with a temperature change of 25 °C ± 5 °C, an exhumation thickness of 0.83 ± 0.16 km, and an exhumation rate of 0.027 ± 0.005 km/Ma. Therefore, the total thickness of exhumation in the Koktokay Pegmatite Group area since ~150 Ma is approximately 4.43 ± 0.81 km, which is shallower than the crystallization pressure constrained by fluid inclusions in the Koktokay Pegmatite (6.8–11.4 km, Zhou et al., 2015b). The reason for this difference is the lack of calculation of the exhumation thickness during the Late Triassic to Early Cretaceous in the Koktokay Pegmatite Group.

Generally, the calculated exhumed thickness of the Koktokay Pegmatite Group is not conducive to the preservation of rare-metal pegmatites. Furthermore, the Jurassic extensive hydrothermal events and potential exhumation from 220 Ma to 150 Ma also contribute to the damage of the pegmatite group. According to the mineralization model of pegmatites, the rare-metal-mineralized pegmatites usually formed at the distal end in the pegmatite group, especially Li–Rb–Cs mineralized pegmatite. Meanwhile, the Be-mineralized pegmatite formed near the end within the pegmatite group (London, 2018; Dill et al., 2012). The preservation history of the Koktokay Pegmatite coincided with the exploration situation, that is, the scale of Li–Rb–Cs-type pegmatite in Koktokay is limited, while that of Be-type pegmatite is huge. In addition, thermochronology study suggest a bad prospect for Li–Rb–Cs-type pegmatite exploration in the Late Triassic Koktokay Pegmatite Group.

5 Conclusion

In this contribution, the samples of the No. 3 pegmatite and the Aler granitic batholith are collected and a series of low-temperature thermochronology analyses and thermal history modelling were applied to explore the denudation and exhumation history of the Koktokay rare-metal pegmatite group and further to provide guidance for subsequent exploitation in this region.

It clearly shows a consistent younger trend of our low-temperature thermochronology apparent ages from the high to low closure temperature of different thermochronology tools, with an apatite U–Pb age of ~176 Ma, a ZFT age of ~150 Ma, a ZHe age of ~70 Ma, an AFT age of ~60 Ma, and an AHe age of 50 Ma. The thermal history modeling results present that the Koktokay Pegmatite Group went through two predominant phases of rapid cooling, occurring in the Middle Jurassic to the Early Cretaceous and the Middle-to-Late Cretaceous. The earlier phase is coupled with the cooling event in the whole Altai and the extensive hydrothermal event in the Koktokay area. The disturbances caused by multiple thermal events make it impossible to calculate exhumation thickness during this stage, but they can be determined to be harmful to the preservation of pegmatite. The later phase would be related to the activity of the Kalaxianger Fault and a series of far-field tectonic events (such as the collapse of the Mongol–Okhotsk Orogen to the east and slab rollback in the Tethys Ocean to the south). A total of ~4.43 ± 0.81 km has been denuded since ~150 Ma, with the Middle-to-Late Cretaceous period accounting for the majority of denudation. Overall, the denudation of the Koktokay Pegmatite Group is relatively intense, which is unfavorable for the preservation of rare-metal pegmatite bodies.

Data availability statement

The original contributions presented in the study are included in the article/supplementary material; further inquiries can be directed to the corresponding author.

Author contributions

WH: Conceptualization, Formal Analysis, Investigation, Methodology, Resources, Software, Validation, Writing – original draft, Writing – review and editing. RG: Funding acquisition, Project administration, Writing – review and editing. TY: Data curation, Funding acquisition, Project administration, Resources, Supervision, Writing – original draft, Writing – review and editing. ZH: Funding acquisition, Supervision, Writing – review and editing. LZ: Writing – review and editing, Investigation. HZ: Conceptualization, Writing – review and editing.

Funding

The author(s) declare that financial support was received for the research and/or publication of this article. This work was financially supported by the China Geological Survey Project (Grant No. DD20240033) and the National Science Foundation of China (Grant Nos. 91962222 and 41773053).

Conflict of interest

The authors declare that the research was conducted in the absence of any commercial or financial relationships that could be construed as a potential conflict of interest.

Generative AI statement

The author(s) declare that no Generative AI was used in the creation of this manuscript.

Any alternative text (alt text) provided alongside figures in this article has been generated by Frontiers with the support of artificial intelligence and reasonable efforts have been made to ensure accuracy, including review by the authors wherever possible. If you identify any issues, please contact us.

Publisher's note

References

Annikova, I. Y., Vladimirov, A., Vystavnoi, S., Zhuravlev, D., Kruk, N., Lepekhina, E., et al. (2006). U-Pb and ^{39}Ar/^{40}Ar dating and Sm-Nd and Pb-Pb isotopic study of the kalguty molybdenum-tungsten ore-magmatic system (south ern Altai). *Petrology* 14, 81–97. doi:10.1134/s0869591106010073

Annikova, I. Y., Vladimirov, A., Smirnov, S. Z., and Gavryushkina, O. A. (2016a). Geology and mineralogy of the alakha spodumene granite porphyry deposit, gorny Altai, Russia. *Russ. Geol. Ore Depos.* 58, 404–426. doi:10.1134/s1075701516050020

Annikova, I. Y., Vladimirova, A. G., Smirnov, S. Z., and Gavryushkina, O. A. (2016b). Geology and mineralogy elaginskogo deposits of spodumene granite-porphyry (gorny Altai, Russia). *Geol. Rudn. Mestorozhd* 58, 451–475.

Bellemans, F., De^Corte, F., and Van Den^Haute, P. (1995). Composition of SRM and CN U-doped glasses: significance for their use as thermal neutron fluence monitors in fission track dating. *Radiat. Meas.* 24 (2), 153–160. doi:10.1016/1350-4487(94)00100-f

BGMRX (1993). *Bureau of geology and mineral resources of xingjiang autonomous region. Regional geology of Xinjiang autonomous region*. Beijing: Geological Publishing House.

Briggs, S. M., Yin, A., Manning, C. E., Chen, Z. L., Wang, X. F., and Grove, M. (2007). Late Paleozoic tectonic history of the Ertix Fault in the Chinese Altai and its implications for the development of the Central Asian Orogenic System. *Geol. Soc. Am. Bull.* 119, 944–960. doi:10.1130/b26044.1

Briggs, S. M., Yin, A., Manning, C. E., Chen, Z. L., and Wang, X. F. (2009). Tectonic development of the Southern Chinese Altai range as determined by structural geology, Thermobarometry, ^{40}Ar-^{39}Ar thermochronology, and Th/Pb ion-Microprpbe Monazite geochronology. *Geol. Soc. Am. Bull.* 121 (9-10), 1381–1393. doi:10.1130/b26385.1

Buslov, M. M. (2011). Tectonics and geodynamics of the Central Asian Foldbelt: the role of late Paleozoic large-amplitude strike-slip faults. *Russ. Geol. Geophys.* 52, 52–71. doi:10.1016/j.rgg.2010.12.005

Buslov, M. M., Saphonova, I. Y., Watanabe, T., Obut, O. T., Fujiwara, Y., Iwata, K., et al. (2001). Evolution of the Paleo-Asian Ocean (Altai-Sayan Region, Central Asia) and collision of possible Gondwana derived terranes with the southern marginal part of the Siberian continent. *Geosciences J.* 5, 203–224. doi:10.1007/bf02910304

Buslov, M. M., Watanabe, T., Fujiwara, Y., Iwata, K., Smirnova, L. V., Yu, S. I., et al. (2004). Late Paleozoic faults of the Altai region, Central Asia: tectonic pattern and model of formation. *J. Asian Earth Sci.* 23, 655–671. doi:10.1016/s1367-9120(03)00131-7

Cai, K., Sun, M., Yuan, C., Xiao, W., Zhao, G., Long, X., et al. (2012). Carboniferous mantle-derived felsic intrusion in the Chinese Altai, NW China: implications for geodynamic change of the accretionary orogenic belt. *Gondwana Res.* 22, 681–698. doi:10.1016/j.gr.2011.11.008

Cao, M. J., Zhou, Q. F., Qin, K. Z., Tang, D. M., and Evans, N. J. (2013). The tetrad effect and geochemistry of apatite from the Altay Koktokay no. 3 pegmatite, Xinjiang, China: implications for pegmatite petrogenesis. *Min. Petrol* 107, 985–1005. doi:10.1007/s00710-013-0270-x

Caves, J. K., Sjostrom, D. J., Mix, H. T., Winnick, M. J., and Chamberlain, C. P. (2014). Aridification of Central Asia and uplift of the Altai and Hangay Mountains, Mongolia: stable isotope evidence. *Am. J. Sci.* 314, 1171–1201. doi:10.2475/08.2014.01

Caves, J. K., Bayshashov, B. U., Zhamangara, A., Ritch, A. J., Ibarra, D. E., Sjostrom, D. J., et al. (2017). Late miocene uplift of the Tian Shan and Altai and reorganization of Central Asia climate. *GSA Today* 27, 20–26. doi:10.1130/GSATG305A.1

Černý, P. (1991). Rare-element granite pegmatites. Part I: anatomy and internal evolution of pegmatite deposits. *Geosci. Can.* 18, 49–67. Available online at: https://journals.lib.unb.ca/index.php/GC/article/view/3722.

Černý, P., and Ercit, T. S. (2005). The classification of granitic pegmatites revisited. *Can. Mineralogist* 43, 2005–2026. doi:10.2113/gscanmin.43.6.2005

Chai, F. M., Dong, L. H., Yang, F. Q., Liu, F., Gen, X. X., and Huang, C. K. (2010). Age, geochemistry and petrogenesis of Tiemierte granites in the Kelang basin at the southern margin of Altay, Xinjiang. *Acta Petrol. Sin.* 26 (2), 377–386.

Che, X. D., Wu, F. Y., Wang, R. C., Gerdes, A., Ji, W. Q., Zhao, Z. H., et al. (2015). *In situ* U-Pb isotopic dating of columbite–tantalite by LA–ICP–MS. *Ore Geol. Rev.* 65, 979–989. doi:10.1016/j.oregeorev.2014.07.008

Chen, B., and Jahn, B. M. (2002). Geochemical and isotopic studies of the sedimentary and granitic rocks of the Altai Orogen of Northwest China and their tectonic implications. *Geol. Mag.* 139, 1–13. doi:10.1017/s0016756801006100

Chew, D. M., Babechuk, M. G., Cogne, N., Mark, C., O'Sullivan, G. J., Henrichs, I. A., et al. (2016). LA-Q-ICPMS trace-element analyses of Durango and McClure Mountain apatite and implications for making natural LA-ICPMS mineral standards. *Chem. Geol.* 435, 35–48. doi:10.1016/j.chemgeo.2016.03.028

De Grave, J., Buslov, M. M., and Van den haute, P. (2007). Distant effects of India-Eurasia convergence and Mesozoic intracontinental deformation in Central Asia: constraints from apatite fission-track thermochronology. *J. Asian Earth Sci.* 29, 188–204. doi:10.1016/j.jseaes.2006.03.001

De Grave, J., Van den Haute, P., Buslov, M. M., Dehandschutter, B., and Glorie, S. (2008). Apatite fission-track thermochronology applied to the Chulyshman Plateau, Siberian Altai Region. *Radiat. Meas.* 43 (1), 38–42. doi:10.1016/j.radmeas.2007.11.068

De Grave, J., Buslov, M. M., Van Den Haute, P., Metcalf, J., Dehandschutter, B., and McWilliams, M. O. (2009). Multi-method chronometry of the Teletskoye graben and its basement, Siberian Altai Mountains: new insights on its thermo-tectonic evolution. *Geol. Soc. Lond. Spec. Publ.* 324 (1), 237–259. doi:10.1144/sp324.17

De Grave, J., Glorie, S., Buslov, M. M., Stockli, D. F., McWilliams, M. O., Batalev, V. Y., et al. (2013). Thermo-tectonic history of the Issyk-Kul basement (Kyrgyz Northern Tien Shan, Central Asia). *Gondwana Res.* 23 (3), 998–1020. doi:10.1016/j.gr.2012.06.014

Dilek, Y., and Furnes, H. (2009). Structure and geochemistry of Tethyan ophiolites and their petrogenesis in subduction rollback systems. *Lithos* 113 (1), 1–20. doi:10.1016/j.lithos.2009.04.022

Dill, H. G. (2016). The CMS classification scheme (Chemical composition-Mineral assemblage-structural geology)-linking geology to mineralogy of pegmatitic and aplitic rocks. *Neues Jahrb. für Mineralogie-Abhandlungen. J. Mineral. Geochem.* 193 (3), 231–263. doi:10.1127/njma/2016/0304

Dill, H. G., Skoda, R., Weber, B., Berner, Z. A., Muller, A., and Bakker, J. R. (2012). A newly discovered swarm of shear-zone-hosted Bi-As-Fe-Mg-P-rich aplites and pegmatites in the hagendorf-pleystein pegmatite province, Southeastern Germany: a step closer to the metamorphic root of pegmatites. *Can. Mineralogist* 50, 943–974. doi:10.3749/canmin.50.4.943

Donelick, R. A., O'Sullivan, P. B., and Ketcham, R. A. (2005). Apatite fission-track analysis. *Rev. Mineralogy Geochem.* 58 (1), 49–94. doi:10.2138/rmg.2005.58.3

Enkelmann, E., and Garver, J. I. (2016). Low-temperature thermochronology applied to ancient settings. *J. Geodyn.* 93, 17–30. doi:10.1016/j.jog.2015.11.001

Evans, N. J., McInnes, B. I., McDonald, B., Danisik, M., Jourdan, F., Mayers, C., et al. (2013). Emplacement age and thermal footprint of the diamondiferous Ellendale E9 lamproite pipe, Western Australia. *Miner. Deposita* 48, 413–421. doi:10.1007/s00126-012-0430-7

Farley, K. A., Wolf, R. A., and Silver, L. T. (1996). The effects of long alpha-stopping distances on (U-Th)/He ages. *Geochimica Cosmochimica Acta* 60, 4223–4229. doi:10.1016/s0016-7037(96)00193-7

Flowers, R. M., Ketcham, R. A., Shuster, D. L., and Farley, K. A. (2009). Apatite (U–Th)/He thermochronometry using a radiation damage accumulation and annealing model. *Geochimica Cosmochimica Acta* 73, 2347–2365. doi:10.1016/j.gca.2009.01.015

Fu, C., Liang, G. H., Xu, X. W., Cai, X. P., Wu, W., Li, Z. Y., et al. (2010). Magnetotelluric study on the Kalaxianger fault zone in the north margin of Junggar, Xinjiang, China. *Acta Petrol. Sin.* 26 (10), 3007–3016.

Garver, J. I. (2003). Etching zircon age standards for fission-track analysis. *Radiat. Meas.* 37 (1), 47–53. doi:10.1016/s1350-4487(02)00127-0

Gautheron, C., Barbarand, J., Ketcham, R. A., Tassan-Got, L., van der Beek, P., Pagel, M., et al. (2013). Chemical influence on α-recoil damage annealing

in apatite: implications for (U–Th)/He dating. *Chem. Geol.* 351, 257–267. doi:10.1016/j.chemgeo.2013.05.027

Gillespie, J., Glorie, S., Jepson, G., Xiao, W. J., and Collins, A. S. (2020). Late Paleozoic exhumation of the West Junggar Mountains, NW China. *J. Geophys. Res. Solid Earth* 125 (1), e2019JB018013. doi:10.1029/2019jb018013

Gillespie, J., Glorie, S., Jepson, G., Zhimulev, F. I., Gurevich, D., Danisik, M., et al. (2021). Inherited structure as a control on late Paleozoic and Mesozoic exhumation of the tarbagatai Mountains, southeastern Kazakhstan. *J. Geol. Soc.* 178 (6), jgs2020–121. doi:10.1144/jgs2020-121

Glorie, S., and De Grave, J. (2016). Exhuming the meso-cenozoic Kyrgyz tianshan and Siberian altai-Sayan: a review based on low-temperature thermochronology. *Geosci. Front.* 7 (2), 155–170. doi:10.1016/j.gsf.2015.04.003

Glorie, S., De Grave, J., Buslov, M. M., Zhimulev, F. I., Izmer, A., Vandoorne, W., et al. (2011). Formation and Palaeozoic evolution of the Gorny-Altai–altai-Mongolia suture zone (south siberia): zircon U/Pb constraints on the igneous record. *Gondwana Res.* 20 (2), 465–484. doi:10.1016/j.gr.2011.03.003

Glorie, S., De Grave, J., Buslov, M. M., Zhimulev, F. I., Elburg, M. A., and Van den daute, P. (2012). Structural control on meso-cenozoic tectonic reactivation and denudation in the Siberian Altai: insights from multi-method thermochronometry. *Tectonophysics* 544-545, 75–92. doi:10.1016/j.tecto.2012.03.035

Glorie, S., Otasevic, A., Gillespie, J., Jepson, G., Danišík, M., Zhimulev, F. I., et al. (2019). Thermo-tectonic history of the junggar alatau within the Central Asian orogenic Belt (SE Kazakhstan, NW China): insights from integrated apatite U/Pb, fission track and (U–Th)/He thermochronology. *Geosci. Front.* 10 (6), 2153–2166. doi:10.1016/j.gsf.2019.05.005

Glorie, S., Nixon, A. L., Jepson, G., Gillespie, J., Warren, C., Meeuws, F., et al. (2023). Meso-cenozoic tectonic history of the Altai: new insights from apatite U-Pb and fission track thermochronology for the Fuyun area (Xinjiang, China). *Tectonics* 42, e2022TC007692. doi:10.1029/2022tc007692

Glover, A. S., Rogers, W. Z., and Barton, J. E. (2012). Granitic pegmatites: storehouses of industrial minerals. *Elements* 8, 269–273. doi:10.2113/gselements.8.4.269

Goeadow, A., Harrison, M., Kohn, B., Lugo-Zazueta, R., and Phillips, D. (2015). The fish canyon tuff: a new look at an old low-temperature thermochronology standard. *Earth Planet. Sci. Lett.* 424, 95–108. doi:10.1016/j.epsl.2015.05.003

Guenthner, W. R., Reiners, P. W., Ketcham, R. A., Nasdala, L., and Giester, G. (2013). Helium diffusion in natural Zircon: radiation damage, anisotropy, and the interpretation of Zircon (U-Th)/He Thermochronology. *Am. J. Sci.* 313 (3), 145–198. doi:10.2475/03.2013.01

Han, B. F. (2008). A preliminary comparison of Mesozoic granitoids and rare metal deposits in Chinese and Russian Mountains. *Acta Petrol. Sin.* 24 (4), 655e660.

He, Z. Y., Wang, B., Glorie, S., Su, W. B., Ni, X. H., Jepson, G., et al. (2022). Mesozoic building of the Eastern Tianshan and East Junggar (NW China) revealed by low-temperature thermochronology. *Gondwana Res.* 103, 37–53. doi:10.1016/j.gr.2021.11.013

House, M. A., Farley, K. A., and Stockli, D. (2000). Helium chronometry of apatite and titanite using Nd-YAG laser heating. *Earth Planet. Sci. Lett.* 183 (3-4), 365–368. doi:10.1016/s0012-821x(00)00286-7

Hu, A. Q., Jahn, B. M., Zhang, G. X., Chen, Y. B., and Zhang, Q. F. (2000). Crustal evolution and Phanerozoic crustal growth in northern Xinjiang: nd isotopic evidence. Part I. Isotopic characterization of basement rocks. *Tectonophysics* 328 (1-2), 15–51. doi:10.1016/s0040-1951(00)00176-1

Huntington, K. W., and Klepeis, K. A. (2018). *Challenges and opportunities for research in tectonics: understanding deformation and the processes that link Earth systems, from geologic time to human time. A community vision document submitted to the U.S. National Science Foundation*. Washington, United States: University of Washington.

Hurford, A. J. (1990). Standardization of fission track dating calibration: recommendation by the Fission Track Working Group of the IUGS Subcommission on Geochronology. *Chem. Geol. Isot. Geosci. Sect.* 80 (2), 171–178. doi:10.1016/0168-9622(90)90025-8

Hurford, A. J., and Green, P. F. (1983). The zeta age calibration of fission-track dating. *Chem. Geol.* 41, 285–317. doi:10.1016/s0009-2541(83)80026-6

Irber, W. (1999). The lanthanide tetrad effect and its correlation with K/Rb, Eu/Eu*, Sr/Eu, Y/Ho and Zr/Hf of evolving peraluminous granite suites. *Geochim. Cosmochim. Acta* 63, 489–508. doi:10.1016/s0016-7037(99)00027-7

Jahns, R. H., and Burnham, C. W. (1969). Experimental studies of pegmatite genesis; l, A model for the derivation and crystallization of granitic pegmatites. *Econ. Geol.* 64, 843–864. doi:10.2113/gsecongeo.64.8.843

Jepson, G., Glorie, S., Konopelko, D., Gillespie, J., Danisik, M., Mirkamalov, R., et al. (2018). Low-Temperature thermochronology of the Chatkal-Kurama Terrane (Uzbekistan-Tajikistan): insights into the meso-cenozoic thermal history of the Western Tian Shan. *Tectonics* 37 (10), 3954–3969. doi:10.1029/2017tc004878

Jepson, G., Glorie, S., Khudoley, A. K., Malyshev, S. V., Gillespie, J., Glasmacher, U. A., et al. (2021). The Mesozoic exhumation history of the Karatau-Talas range, western Tian Shan, Kazakhstan-Kyrgyzstan. *Tectonophysics* 814 (5), 228977. doi:10.1016/j.tecto.2021.228977

Jolivet, M., Ritz, J. F., Vassallo, R., Larroque, C., Braucher, R., Todbileg, M., et al. (2007). Mongolian summits: an uplifted, flat, old but still preserved erosion surface. *Geology* 35 (10), 871–874. doi:10.1130/g23758a.1

Jolivet, M., De Boisgrollier, T., Petit, C., Fournier, M., Sankov, V. A., Ringenbach, J. C., et al. (2009). How old is the Baikal Rift Zone? Insight from apatite fission track thermochronology. *Tectonics* 28 (3), 2008TC002404. doi:10.1029/2008tc002404

Kesler, S. E., and Wilkinson, B. H. (2006). The role of exhumation in the temporal distribution of ore deposits. *Econ. Geol.* 101 (5), 919–922. doi:10.2113/gsecongeo.101.5.919

Ketcham, R. A. (2005). Forward and inverse modeling of low-temperature thermochronometry data. *Rev. Mineralogy Geochem.* 58 (1), 275–314. doi:10.2138/rmg.2005.58.11

Ketcham, R. A., Carter, A., Donelick, R. A., Barbarand, J., and Hurford, A. J. (2007). Improved modeling of fission-track annealing in apatite. *Am. Mineralogist* 92 (5-6), 799–810. doi:10.2138/am.2007.2281

Khromykh, S. V., Oitseva, T. A., Kotler, P. D., D'yachkov, B. A., Smirnov, S. Z., Travin, A. V., et al. (2020). Rare-metal pegmatite deposits of the Kalba Region, Eastern Kazakhstan: age, composition and petrogenetic implications. *Minerals* 10, 1017. doi:10.3390/min10111017

Laurent-Charvet, S., Charvet, J., Shu, L., Ma, R., and Lu, H. (2002). Palaeozoic Late collisional strike-slip deformations in Tianshan and Altay, Eastern Xinjiang, NW China. *Terra Nova* 14 (4), 249–256. doi:10.1046/j.1365-3121.2002.00417.x

Li, P., Yuan, C., Sun, M., Long, X., and Cai, K. (2015). Thermochronological constraints on the late Paleozoic tectonic evolution of the southern Chinese Altai. *J. Asian Earth Sci.* 113, 51–60. doi:10.1016/j.jseaes.2014.11.004

Li, P., Sun, R., Rosenbaum, G., Jourdan, F., Li, S., and Cai, K. (2017). Late Paleozoic closure of the Ob-Zaisan Ocean along the Irtysh shear zone (NW China): implications for arc amalgamation and orolinal bending in the Central Asian orogenic belt. *Geol. Soc. Am. Bull.* 219 (5-6), 547–569. doi:10.1130/b31541.1

Li, P. F., Sun, M., Shu, C. T., Yuan, C., Jiang, Y. D., Zhang, L., et al. (2019). Evolution of the Central Asian Orogenic Belt along the Siberian margin from Neoproterozoic-Early Paleozoic accretion to Devonian trench retreat and a comparison with Phanerozoic eastern Australia. *Earth-Science Rev.* 198, 102951. doi:10.1016/j.earscirev.2019.102951

Li, C., Li, Z., Zeng, M., and Stern, R. J. (2022). Early Eocene A-type (ferroan) rhyolites in southwestern Tibet: a far-field tectonic effect of the India–Eurasia collision. *Int. Geol. Rev.* 65, 2047–2066. doi:10.1080/00206814.2022.2117740

Linnen, R. L., Van Lichtervelde, M., and Černý, P. (2012). Granitic pegmatites as sources of strategic metals. *Elements* 8, 275–280. doi:10.2113/gselements.8.4.275

Linnen, R. L., Samson, I. M., Williams-Jones, A. E., and Chakhmouradian, A. R. (2014). "Geochemistry of the rare-earth element, Nb, Ta, Hf, and Zr deposits," in *Treatise on geochemistry*. Editor H. D. H. K. Turekian Second Edition (Oxford: Elsevier), 543–568.

Liu, F., and Han, D. (2019). Petrogenetic and tectonic implications of Triassic granitoids in the Chinese Altay: the Alaer granite example. *Heliyon* 5, e01261. doi:10.1016/j.heliyon.2019.e01261

Liu, F., Zhang, Z. X., Li, Q., Qu, W. J., and Li, C. (2012). New age constraints of Keketuohai pegmatite No.3 vein, Altay mountains, Northwest China: from the evidence of Re-Os and U-Pb dating. *Mineral. Deposits* 31 (5), e1111–e1118. doi:10.3969/j.issn.0258-7106.2012.05.013

Liu, F., Zhang, Z. X., Li, Q., Zhang, C., and Li, C. (2014). New precise timing constraint for the Keketuohai No. 3 pegmatite in Xinjiang, China, and identification of its parental pluton. *Ore Geol. Rev.* 56, 209–219. doi:10.1016/j.oregeorev.2013.08.020

Liu, D. Y., Li, G. W., Xu, Z. Q., Zhu, W. B., Gao, J. G., Zheng, B. H., et al. (2023). Exhumation of Jiajika lithium deposit in the eastern Tibetan Plateau: insights from low-temperature thermochronology of the JJK scientific drilling borehole. *Ore Geol. Rev.* 160, 105575. doi:10.1016/j.oregeorev.2023.105575

London, D. (2008). *Pegmatite*. Ottawa, Canada: Mineralogical Association of Canada.

London, D. (2014). A petrologic assessment of internal zonation in granitic pegmatites. *Lithos* 184–187, 74–104. doi:10.1016/j.lithos.2013.10.025

London, D. (2018). Ore-forming processes within granitic pegmatites. *Ore Geol. Rev.* 101, 349–383. doi:10.1016/j.oregeorev.2018.04.020

Lv, Z. H., Zhang, H., Tang, Y., and Guan, S. J. (2012). Petrogenesis and magmatic-hydrothermal evolution time limitation of Kelumute No. 112 pegmatite in Altay, Northwestern China: evidence from zircon U-Pb and Hf isotopes. *Lithos* 154, 374–391. doi:10.1016/j.lithos.2012.08.005

Lv, Z. H., Zhang, H., Tang, Y., Liu, Y. L., and Zhang, X. (2018). Petrogenesis of syn-orogenic rare metal pegmatites in the Chinese Altai: evidences from geology, mineralogy, zircon U-Pb age and Hf isotope. *Ore Geol. Rev.* 95, 161–181. doi:10.1016/j.oregeorev.2018.02.022

Ma, L., Wang, D., Li, Z. X., Wyman, D. A., Jiang, Z. Q., Yang, J. H., et al. (2013). Early Late Cretaceous (ca. 93Ma) norites and hornblendites in the Milin area, eastern Gangdese: Lithosphere–Asthenosphere interaction during slab roll-back and an insight into early Late Cretaceous (ca. 100–80Ma) magmatic "flare-up" in southern lhasa (tibet). *Lithos* 172-173, 17–30. doi:10.1016/j.lithos.2013.03.007

Ma, Z. L., Zhang, H., Tang, Y., Lv, Z. H., Zhang, X., and Zhao, J. Y. (2015). Zircon U-Pb geochronology and Hf isotopes of pegmatites from the kaluan mining area in the altay, Xinjiang and their genetic relationship with the halong granite. *Geochimica* 44, 9–26. doi:10.19700/j.0379-1726.2015.01.002

Marton, I., Moritz, R., and Spikings, R. (2010). Application of low-temperature thermochronology to hydrothermal ore deposits: formation, preservation and exhumation of epithermal gold systems from the eastern rhodopes, Bulgaria. *Tectonophysics* 483, 240–254. doi:10.1016/j.tecto.2009.10.020

Masuda, A., Matsuda, N., Minami, M., and Yamamoto, H. (1994). Approximate estimation of the degree of lanthanide tetrad effect from precise but partially void data measured by isotope dilution and an electron configuration model to explain the tetrad phenomenon. *Proc. Jpn. Acad.* 70B, 169–174. doi:10.2183/pjab.70.169

McDannell, K. T. (2020). *Notes on statistical age dispersion in fission-track datasets: the chi-square test, annealing variability, and analytical considerations. Earth ArXiv*. doi:10.31223/osf.io/uj4hx

McDannell, K. T., Zeitler, P. K., and Idleman, B. D. (2018). Relict topography within the hangay Mountains in central Mongolia: quantifying long-term exhumation and relief change in an old landscape. *Tectonics* 37 (8), 2531–2558. doi:10.1029/2017tc004682

Metelkin, D. V., Vernikovsky, V. A., and Kazansky, A. Y. (2012). Tectonic evolution of the Siberian paleocontinent from the Neoproterozoic to the late Mesozoic: paleomagnetic record and reconstructions. *Russ. Geol. Geophys.* 53 (7), 675–688. doi:10.1016/j.rgg.2012.05.006

Molnar, P., and Tapponnier, P. (1975). Cenozoic tectonics of Asia: effects of a Continental collision: features of recent Continental tectonics in Asia can be interpreted as results of the india-eurasia collision. *Science* 189, 419–426. doi:10.1126/science.189.4201.419

Murzintsev, N. G., Annikova, I. Y., Travin, A. V., Vladimirov, A. G., Dyachkov, B. A., Maslov, V. I., et al. (2019). Thermochronology and mathematical modeling of the formation dynamics of rare-metal-granite deposits of the Altai collision system. *Geodyn. and Tectonophys.* 10, 375–404. doi:10.5800/gt-2019-10-2-0419

Pullen, A., Banaszynski, M., Kapp, P., Thomson, S. N., and Cai, F. (2020). A mid-cretaceous change from fast to slow exhumation of the Western Chinese Altai Mountains: a climate driven exhumation signal? *J. Asian Earth Sci.* 197, 104387. doi:10.1016/j.jseaes.2020.104387

Reiners, P. W., and Brandon, M. T. (2006). Using thermochronology to understand orogenic erosion. *Annu. Rev. Earth Planet. Sci.* 34, 419–466. doi:10.1146/annurev.earth.34.031405.125202

Shen, P., Pan, H. D., Li, C. H., Feng, H. X., He, L. F., Bai, Y. X., et al. (2022). Newly-recognized Triassic highly fractionated leucogranite in the koktokay deposit (altai, China): Rare-metal fertility and connection with the no. 3 pegmatite. *Gondwana Res.* 112, 24–51. doi:10.1016/j.gr.2022.09.007

Simmons, W. B., Pezzotta, F., Shigley, J. E., and Beurlen, H. (2012). Granitic pegmatites as sources of colored gemstones. *Elements* 8, 281–287. doi:10.2113/gselements.8.4.281

Simmons, W. B., Falster, A. U., and Gary, F. (2020). The Plumbago North pegmatite, Maine, USA: a new potential lithium resource. *Miner. Deposita* 55, 1505–1510. doi:10.1007/s00126-020-00956-y

Sobel, E. R., Chen, J., and Heermance, R. V. (2006). Late Oligocene-Early Miocene initiation of shortening in the Southwestern Chinese tian Shan: implications for Neogene shortening rate variations. *Earth Planet. Sci. Lett.* 247 (1), 70–81. doi:10.1016/j.epsl.2006.03.048

Sun, M., Yuan, C., Xiao, W. J., Long, X. P., Xia, X. P., Zhao, G. C., et al. (2008). Zircon U-Pb and Hf isotopic study of gneissic rocks from the Chinese Altai: progressive accretionary history in the early to middle Palaeozoic. *Chem. Geol.* 247, 352–383. doi:10.1016/j.chemgeo.2007.10.026

Tagami, T., Galbraith, R. F., and Yamada, R. (1998). "Revised annealing kinetics of fission tracks in zircon and geological implications," in *Advances in fission-track geochronology* (Dordrecht: Springer), 99–112.

Tang, Y., Wang, H., Zhang, H., and Lv, Z. H. (2018). K-feldspar composition as an exploration tool for pegmatite-type rare metal deposits in Altay, NW China. *J. Geochem. Explor.* 185, 130–138. doi:10.1016/j.gexplo.2017.11.015

Thomas, R., and Davidson, P. (2015). Comment on "A petrologic assessment of internal zonation in granitic pegmatites" by David London (2014). *Lithos* 212–215, 462–468. doi:10.1016/j.lithos.2014.08.028

Tong, L. X., Chen, Y. B., Xu, Y. G., Zhou, X., and Liu, Z. (2013). Zircon ages of the ultrahigh-temperature metapelitic granulite from the Altai orogen, NW China, and geological implications. *Acta Petrol. Sin.* 29 (10), 3435–3445.

Tong, L. X., Xu, Y. G., Cawood, P. A., Zhou, X., Chen, Y. B., and Liu, Z. (2014). Anticlockwise P-T evolution at ~280 Ma recorded from ultrahigh-temperature metapelitic granulite in the Chinese Altai orogenic belt, a possible link with the Tarim mantle plume? *J. Asian Earth Sci.* 94, 1–11. doi:10.1016/j.jseaes.2014.07.043

Tong, Y., Wang, T., Jahn, B., Sun, M., Hong, D. W., and Gao, J. F. (2014). Post-accretionary Permian granitoids in the Chinese Altai orogen: geochronology, petrogenesis and tectonic implications. *Am. J. Sci.* 314 (1), 80–109. doi:10.2475/01.2014.03

Vassallo, R., Jolivet, M., Ritz, J. F., Braucher, R., Larroque, C., Sue, C., et al. (2007). Uplift age and rates of the Gurvan Bogd system (Gobi-Altay) by apatite fission track analysis. *Earth Planet. Sci. Lett.* 259 (3-4), 333–346. doi:10.1016/j.epsl.2007.04.047

Vermeesch, P. (2009). RadialPlotter: a java application for fission track, luminescence and other radial plots. *Radiat. Meas.* 44, 409–410. doi:10.1016/j.radmeas.2009.05.003

Vladimirov, A. G., Kruk, N. N., Polyanskii, O. P., Vladimirov, V. G., Babin, G. A., Rudnev, S. N., et al. (2005). Correlation of Hercy nian deformations, sedimentation and magmatism in the Altai collisional system as reflecting plate- and plum-tectonics. *Prob. Tect. Cent. Asia Mosc. Geos.* 1277, e1308.

Wang, T., Hong, D. W., Jahn, B. M., Tong, Y., Wang, Y., Han, B., et al. (2006). Timing, petrogenesis, and setting of Paleozoic synorogenic intrusions from the Altai Mountains, Northwest China: implications for the tectonic evolution of an accretionary orogen. *J. Geol.* 114, 735–751. doi:10.1086/507617

Wang, T., Tong, Y., Jahn, B. M., Zou, T. R., Wang, Y. B., Hong, D. W., et al. (2007). SHRIMP U-Pb Zircon geochronology of the Altai no. 3 Pegmatite, NW China, and its implications for the origin and tectonic setting of the pegmatite. *Ore Geol. Rev.* 32, 325–336. doi:10.1016/j.oregeorev.2006.10.001

Wang, T., Tong, Y., Li, S., Zhang, J. J., Shi, X. J., Li, J. Y., et al. (2010). Spatial and temporal variations of granitoids in the Altay Orogen and their implications for tectonic setting and crustal growth: perspectives from Chinese Altay. *Acta Petrological Mineralogical* 29 (6), 595.

Wang, Y. Z., Wu, C. D., Ma, J., Fang, Y. N., Xu, Z., and Zhou, Y. X. (2019). Strata color rhythm of the Cretaceous-Neogene and evolution of palaeoenvironment and palaeoclimate in Junggar Basin. *J. Palaeogeogr.* 21 (3), 451–468. [in Chinese with English abstract].

Webber, K., William, B. S., Falster, A. U., and Hanson, S. (2019). Anatectic pegmatites of the Oxford County pegmatite field, Maine, USA. *Can. Mineralogist* 57 (5), 811–815. doi:10.3749/canmin.ab00028

Windley, B. F., Alexeiev, D., Xiao, W. J., Kröner, A., and Badarch, G. (2007). Tectonic models for accretion of the Central Asian Orogenic Belt. *J. Geol. Soc.* 164, 31–47. doi:10.1144/0016-76492006-022

Wu, L., Monié, P., Wang, F., Lin, W., Ji, W. B., Bonno, M., et al. (2016). Cenozoic exhumation history of Sulu terrane: implications from (U-Th)/He thermochrology. *Tectonophysics* 672-673, 1–15. doi:10.1016/j.tecto.2016.01.035

Wu, M. X., Yin, J. Y., He, Z. Y., Xiao, W. J., Wang, Y. N., Chen, W., et al. (2023). Mesozoic thermo-tectonic evolution of the Western Altai Orogenic Belt (NW China): insights from low-temperature thermochronology. *Lithosphere* 14, 8161000. doi:10.2113/2023/8161000

Xiao, W. J., Windley, B. F., Huang, B. C., Han, C. M., Yuan, C., Chen, H. L., et al. (2009). End-Permian to mid-triassic termination of the accretionary processes of the southern Altaids: implications for the geodynamic evolution, Phanerozoic continental growth, and metallogeny of Central Asia. *Int. J. Earth Sci.* 98, 1189–1217. doi:10.1007/s00531-008-0407-z

Xiao, W. J., Windley, B. F., Sun, S., Li, J., Huang, B., Han, C., et al. (2015). A tale of amalgamation of three Permo-Triassic collage systems in Central Asia: oroclines, sutures, and terminal accretion. *Annu. Rev. Earth Planet. Sci.* 43, 477–507. doi:10.1146/annurev-earth-060614-105254

Yang, Y. T., Song, C. C., and He, S. (2015). Jurassic tectonostratigraphic evolution of the Junggar basin, NW China: a record of Mesozoic intraplate deformation in Central Asia. *Tectonics* 34, 86–115. doi:10.1002/2014tc003640

Yin, C., Ou, J., Long, X., Huang, F., Zhang, J., Li, S., et al. (2019). Late Cretaceous Neo-Tethyan slab roll-back: evidence from zircon U-Pb-O and whole-rock geochemical and sr-nd-fe isotopic data of adakitic plutons in the Himalaya-Tibetan Plateau. *Geol. Soc. Am. Bull.* 132 (1-2), 409–426. doi:10.1130/b35242.1

Yuan, W. M., Zhang, X. T., Dong, J. Q., Tang, Y. H., Yu, F. S., and Wang, S. C. (2003). A new vision of the intracontinental evolution of the eastern Kunlun Mountains, Northern Qinghai-Tibet plateau, China. *Radiat. Meas.* 36, 357–362. doi:10.1016/s1350-4487(03)00151-3

Yuan, W. M., Carter, A., Dong, J. Q., Bao, Z. K., An, Y. C., and Guo, Z. J. (2006). Mesozoic tertiary exhumation history of the Altai Mountains, northern Xinjiang, China: new constraints from apatite fission track data. *Tectonophysics* 412 (3-4), 183–193. doi:10.1016/j.tecto.2005.09.007

Yuan, C., Sun, M., Xiao, W. J., Chen, H. L., Lin, S. F., Xia, X. P., et al. (2007). Accretionary orogenesis of the Chinese Altai: insights from Paleozoic granitoids. *Chem. Geol.* 242, 22–39. doi:10.1016/j.chemgeo.2007.02.013

Zhai, Y. S., Deng, J., and Peng, R. M. (2000). Research contents and methods for port-ore changes, modifications and preservation. *Earth Sci.* 4, 340–345. doi:10.3321/j.issn:1000-2383.2000.04.002

Zhang, H. (2001). *The geochemical behaviors and mechanisms of incompatible trace elements in the magmatic-hydrothermal transition system: a case study of Altay No.3 pegmatite, Xinjiang. Ph.D. thesis, Institute of Geochemistry*. Guiyang, China: Chinese Academy of Sciences.

Zhang, H., and Li, G. S. (2024). Metallogenic mechanism of the Koktokay pegmatite-type rare-metal deposit, Northwest China. *Acta Petrol. Sin.* 40 (9), 2769–2785. doi:10.18654/1000-0569/2024.09.10

Zhang, Q. F., Hu, A. Q., Zhang, G. X., Fan, S. K., Pu, Z. P., and Li, Q. X. (1994). Isotope age evidence of Mesozoic and Cenozoic magmatic activity in Altai region. *Geochimica* 3, 269–280.

Zhang, Y. F., Lin, X. W., Guo, Q. M., Wang, X., Zhao, D. C., Dang, C., et al. (2015). LA-ICP-MS zircon U-Pb dating and geochemistry of Aral granitic plutons in Koktokay area in the southern Altay margin and their source significance. *Acta Geol. Sin.* 89 (02), 339–354. doi:10.19762/j.cnki.dizhixuebao.2015.02.010

Zhang, J., Wang, T., Tong, Y., Zhang, Z., Song, P., Zhang, L., et al. (2017). Tracking deep ancient crustal components by xenocrystic/inherited zircons of Palaeozoic felsic igneous rocks from the Altai-East Junggar terrane and adjacent regions, western Central Asian Orogenic Belt and its tectonic significance. *Int. Geol. Rev.* 59, 2021–2040. doi:10.1080/00206814.2017.1308841

Zhang, L., Yang, L. Q., Wang, Y., Weinberg, R. F., An, P., and Chen, B. Y. (2017). Thermochronologic constrains on the processes of formation and exhumation of the Xinli orogenic gold deposit, Jiaodong Peninsula, eastern China. *Ore Geol. Rev.* 81, 140–153. doi:10.1016/j.oregeorev.2016.09.026

Zhao, Z. H., and Yan, S. (2023). Some issues relevant to rare metal metallogeny of Granitic pegmatites. [in Chinese with English abstract]. *Geotect. Metallogenia* 2, 1–41. doi:10.16539/j.ddgzyckx.2023.01.001

Zheng, Y., Zhang, L., Li, D. F., Kapsiotis, A., and Chen, Y. J. (2015). Genesis of the Dadonggou Pb-Zn deposit in Kelan basin, Altay, NW China: constraints from zircon U-Pb and biotite ^{40} Ar/^{39} Ar geochronological data. *Ore Geol. Rev.* 64, 128–139. doi:10.1016/j.oregeorev.2014.07.002

Zheng, Y., Chen, Y. J., Cawood, P., Wang, Y. J., Chen, H. Y., Zhang, L., et al. (2017). Late Permian-Triassic metallogeny in the Chinese Altay Orogen: constraints from mica ^{40}Ar/^{39}Ar dating on ore deposits. *Gondwana Res.* 43, 4–16. doi:10.1016/j.gr.2015.08.018

Zhou, Q. F., Qin, K. Z., Tang, D. M., Tian, Y., Cao, M. J., and Wang, C. L. (2015a). Formation age and evolution time span of the Koktokay No. 3 pegmatite, Altai, NW China: evidence from U-Pb zircon and ^{40}Ar/^{39}Ar muscovite ages. *Resour. Geol.* 65, 210–231. doi:10.1111/rge.12067

Zhou, Q. F., Qin, K. Z., Tang, D. M., Wang, C. L., Tian, Y., and Sakyi, P. A. (2015b). Mineralogy of the Koktokay No. 3 pegmatite, Altai, NW China: implications for evolution and melt–fluid processes of rare-metal pegmatites. *Eur. J. Mineralogy* 27 (3), 433–457. doi:10.1127/ejm/2015/0027-2443

Zorin, Y. A. (1999). Geodynamics of the western part of the Mongolia-Okhotsk collisional belt, Trans-Baikal region (Russia) and Mongolia. *Tectonophysics* 306, 33–56. doi:10.1016/s0040-1951(99)00042-6

Zou, T. R., and Li, Q. C. (2006). *Rare and rare earth metallic deposits in Xinjiang*. Beijing, China: Geological Publishing House, 1–284.